

Condensate formation and multiscale dynamics in two-dimensional active suspensionsMoritz Linkmann,^{1,*} M. Cristina Marchetti,² Guido Boffetta,³ and Bruno Eckhardt^{1,†}¹*Fachbereich Physik, Philipps-Universität Marburg, D-35032 Marburg, Germany*²*Department of Physics, University of California, Santa Barbara, California 93106, USA*³*Dipartimento di Fisica and INFN, Università di Torino, via P. Giuria 1, 10125 Torino, Italy*

(Received 17 May 2019; accepted 5 February 2020; published 19 February 2020)

The collective effects of microswimmers in active suspensions result in *active turbulence*, a spatiotemporally chaotic dynamics at mesoscale, which is characterized by the presence of vortices and jets at scales much larger than the characteristic size of the individual active constituents. To describe this dynamics, Navier-Stokes–based one-fluid models driven by small-scale forces have been proposed. Here, we provide a justification of such models for the case of dense suspensions in two dimensions (2D). We subsequently carry out an in-depth numerical study of the properties of one-fluid models as a function of the active driving in view of possible transition scenarios from active turbulence to large-scale pattern, referred to as condensate, formation induced by the classical inverse energy cascade in Newtonian 2D turbulence. Using a one-fluid model it was recently shown [M. Linkmann *et al.*, *Phys. Rev. Lett.* **122**, 214503 (2019)] that two-dimensional active suspensions support two nonequilibrium steady states, one with a condensate and one without, which are separated by a subcritical transition. Here, we report further details on this transition such as hysteresis and discuss a low-dimensional model that describes the main features of the transition through nonlocal-in-scale coupling between the small-scale driving and the condensate.

DOI: [10.1103/PhysRevE.101.022609](https://doi.org/10.1103/PhysRevE.101.022609)**I. INTRODUCTION**

Active suspensions consist of self-propelled constituents, e.g., bacteria such as *Bacillus subtilis* and *Escherichia coli* [1,2], chemically driven colloids [3], or active nematics [4–6] that move in a solvent liquid, most often water. Their collective motion results in complex patterns on many scales, and shows different phases of coherence and self-organization such as swarming, cluster formation, jets, and vortices [2,7–12] and, eventually, *active* or *bacterial turbulence* [2]. The latter is a state characterized by spatiotemporal chaotic dynamics reminiscent of vortex patterns in turbulent flows. The analogy is not complete, though, since Newtonian turbulence is a multiscale phenomenon associated with and dominated by dynamics in an inertial range of scales. Since dissipative effects are negligible in the inertial range, the rate of energy transfer across inertial ranges is constant, and is one of the determining features of the well-known energy cascade [13]. Thus far, the states that have been described as bacterial turbulence do not have an inertial range.

Active and Newtonian turbulence usually occur in different regions of parameter space. With Reynolds numbers $Re = UL/\nu$ based on typical velocities U , lengths L , and the viscosity ν of the liquid, one finds turbulence occurs in pipes and other flows for Reynolds numbers around 2000 [14–16], while the mesoscale vortices observed in bacterial suspensions [2] are associated with a Reynolds number of $O(10^{-3} - 10^{-2})$, far from the inertial dynamics of Newtonian turbulence.

However, rheological measurements of the effective viscosity have shown that the active motion of the constituents can reduce the effective viscosity by about an order of magnitude compared to the solvent viscosity [17–23]. Multiscale states at Reynolds number around 30 have been reported for larger microswimmers such as magnetic rotors [24]. That is, under favorable conditions active suspensions can reach parameter ranges where inertial effects will influence the dynamics, and where a transition from active to inertial turbulence could be achieved.

The effects of inertia are particularly intriguing in two-dimensional (2D) and quasi-two-dimensional suspensions, as kinetic energy is transferred from small to large scales in 2D turbulence, eventually resulting in the accumulation of energy at the largest length scales [25–28]. This phenomenon can be viewed in analogy to Bose-Einstein condensation, which is why the concentration of energy on the largest scales is called the formation of a condensate.

Full models for the dynamics of active suspensions require equations for the velocity field and the swimmers, with suitable couplings between them [29]. Since our focus is on the inertial effects in the flow fields, it is advantageous to eliminate the bacteria and to use equations for the flow fields. Such one-fluid models of active suspensions have recently been proposed [10,30] and have already led to a number of numerical investigations into the nonlinear dynamics of active suspensions that have revealed new phenomena, such as nonuniversality of spectral exponents [31], mirror-symmetry breaking [32], or the formation of vortex lattices [33]. Hints of condensation and multiscaling have been also observed [34,35], but the actual formation of sizable condensates and the connection between 2D active and Newtonian turbulence

*moritz.linkmann@physik.uni-marburg.de

†Deceased.

have not been explored systematically. Using a variant of these one-fluid models we have recently shown that condensates can form in active suspensions, and they do so through a subcritical transition [36]. We here provide further results on this transition and on the multiscale dynamics of dense active suspensions.

This paper is organized as follows. We begin with a general discussion of continuum models for active suspensions in Sec. II, including a justification of Navier-Stokes–based one-fluid models for dense suspensions in 2D. Section III contains a description of the data sets collected in direct numerical simulations (DNS), followed by a discussion of the general features of multiscale dynamics and large-scale pattern formation in one-fluid models of active suspensions in Sec. IV. The subcritical transition to condensate formation is described in detail in Secs. V and VI introduces a low-dimensional model that captures the qualitative features of the transition through a nonlocal-in-scale coupling between the condensate and the driven scales. We summarize our results in Sec. VII.

II. MODELS DESCRIBING BACTERIAL SUSPENSIONS

Active suspensions consist of swimmers immersed in a fluid. Models for such suspensions have to capture the dynamics of the solvent fluid and the motion of the bacteria, which, in a continuum description, leads to a two-fluid approach, where the solvent flow and the polarized motion of the microswimmers are described by separate, but interacting fields. In order to simplify the model, one-fluid descriptions leading to Navier-Stokes–type equations have been proposed [10,11,30,32,37]. Such simplified models are usually obtained in one of two ways: (i) by eliminating the motion of the solvent in favor of the bacterial motion to obtain “bacterial flow models” [10,11,37] or (ii) by eliminating the motion of the bacteria in favor of the fluid flow, resulting in a “solvent flow model” [30,32]. In both cases the resulting velocity field is assumed to be divergence free, which limits the applicability of these models to very dense suspensions where fluctuations in the bacterial density can be neglected [10]. In the next sections, we motivate a single-equation solvent flow model in two dimensions from the general two-fluid approach.

A. Justification of effective models in 2D

At the continuum level, an active bacterial suspension is described by equations for the total density ρ and flow velocity \mathbf{u} of the suspension, the concentration c of bacteria, and a vector field \mathbf{p} describing bacterial motion. A finite value of $|\mathbf{p}|$ also corresponds to polar orientational order of the elongated swimmers, hence \mathbf{p} is generally referred to as bacterial polarization. We assume that the suspension is incompressible, i.e., $\dot{\rho} = 0$, implying $\nabla \cdot \mathbf{u} = 0$, and that the bacterial concentration is constant, resulting in $\nabla \cdot \mathbf{p} = 0$. This then leaves two coupled equations [29], given by

$$\partial_t \mathbf{u} + \mathbf{u} \cdot \nabla \mathbf{u} = -\nabla \Pi + \nabla \cdot \sigma^a + \nu \Delta \mathbf{u}, \quad (1)$$

$$\begin{aligned} \partial_t \mathbf{p} + \mathbf{u} \cdot \nabla \mathbf{p} = & -\nabla \Pi'(|\mathbf{p}|, c) - \lambda_1 \mathbf{p} \cdot \nabla \mathbf{p} + \frac{1}{2} \boldsymbol{\omega} \times \mathbf{p} \\ & + \lambda \mathbf{D} \cdot \mathbf{p} + \frac{1}{\gamma_F} \mathbf{h}, \end{aligned} \quad (2)$$

where Π is the pressure (divided by the total density) which ensures incompressibility of the velocity field, σ^a the active stress that couples bacteria and flow (and that will be discussed further below), Π' is an effective pressure term that depends on the bacterial concentration and the polarization, $\boldsymbol{\omega} = \nabla \times \mathbf{u}$ is the vorticity, $\mathbf{D} = \frac{1}{2}[\nabla \mathbf{u} + (\nabla \mathbf{u})^T]$ the rate of strain tensor, and ν the kinematic viscosity of the solvent. The parameters λ_1 and λ capture advective and flow alignment, and γ_F is a rotational viscosity.

The molecular field \mathbf{h} can be obtained from a free energy F for a polar fluid, modeled similar to a liquid crystal, as the derivative $\mathbf{h} = -\delta F / \delta \mathbf{p}$, where

$$F = \int \left[\frac{\alpha_F}{2} \mathbf{p}^2 + \frac{\beta_F}{4} \mathbf{p}^4 + \frac{K}{2} (\nabla \mathbf{p})^2 \right] dx, \quad (4)$$

with K the liquid crystalline stiffness in a one-elastic constant approximation and α_F and β_F the parameters which determine the onset of a polarized state for $\alpha_F < 0$. Note that we have neglected in both equations passive liquid-crystalline stresses of higher order in gradients of the polarization. A derivation of Eq. (2) can be found, for instance, in Ref. [29].

The feedback of the active swimmers on the flow is contained in the stress tensors σ^a , which results from the active dipolar forces exerted on the solvent by the microswimmers [38]. On length scales large compared to the size of swimmers, it can be expressed through a gradient expansion, with leading-order term

$$\sigma_{ij}^{a(0)} = \alpha (p_i p_j - \frac{1}{3} \delta_{ij} |\mathbf{p}|^2) + O(\nabla), \quad (4)$$

where α is a parameter known as activity, that depends on the concentration of microswimmers, their typical swimming speed, and the type of swimmer. The symbol $O(\nabla)$ indicates higher-order terms that contain gradients of the polarization field. The contribution of the diagonal term $-\frac{1}{3} \delta_{ij} \mathbf{p}^2$ can be absorbed in the pressure gradient in Eq. (1).

Note that the leading-order contribution to the active stress given in Eq. (4) has nematic rather than polar symmetry, as it is parity invariant. Indeed, an active stress with purely polar symmetry arises first in terms containing gradients [39], and is given by

$$\sigma_{ij}^{a(1)} = \beta (\partial_i p_j + \partial_j p_i), \quad (5)$$

where β is another activity parameter that depends, amongst other quantities, on the direction of the polarization field with respect to the swimming direction [29,40].

In most studies of active suspensions, the fluid flow \mathbf{u} is slaved to the polarization field \mathbf{p} , resulting in the Toner-Tu model for the dynamics of the polarization [10]. In contrast, we here wish to eliminate \mathbf{p} in favor of \mathbf{u} in order to obtain an equation for active flows, as done for instance in Ref. [32].

In order to derive such a single-equation model, one has to solve the equation for \mathbf{p} and substitute the solution into the equation for \mathbf{u} . Even though the nonlinearities in (2) make it difficult to obtain an analytical solution, such an approach will generally give a functional relation between \mathbf{p} and \mathbf{u} . In what follows, we show how the 2D solvent model can be obtained as the leading-order contribution for the case of a linear, though not necessarily local, relation between \mathbf{p} and \mathbf{u} ,

of the form

$$p_i[\mathbf{u}](\mathbf{x}, t) = (G_{ij} * u_j)(\mathbf{x}, t), \quad (6)$$

where G_{ij} is a kernel that depends on the details of the system and $*$ denotes a convolution. The derivation follows similar steps as in active scalar advection in geophysical flows [41,42].

In 2D, incompressibility of the fields reduces the number of degrees of freedom of each vector field from two to one, usually given by the out-of-plane vorticities $\omega(x, y) = \hat{z} \cdot (\nabla \times \mathbf{u}(x, y))$ and $m(x, y) = \hat{z} \cdot (\nabla \times \mathbf{p}(x, y))$ of the respective fields, where \hat{z} is a unit vector in the z direction. Equation (6) then becomes a scalar relation

$$m[\omega](\mathbf{x}, t) = (G * \omega)(\mathbf{x}, t). \quad (7)$$

In a dense bacterial suspension, hydrodynamic interactions are screened and the relation between m and ω is expected to be local. We can then assume G to be a sharply peaked function, for instance, proportional to a narrow spherically symmetric 2D Gaussian

$$G(\mathbf{x}) = \frac{A}{\pi a} e^{-|\mathbf{x}|^2/a^2}, \quad (8)$$

with shape parameter $a > 0$ and constant amplitude A . Expanding the Fourier transform of the Gaussian in terms of its shape parameter around zero leads to an expansion of Eq. (7) of the form

$$m[\omega](\mathbf{x}, t) = A\omega(\mathbf{x}, t) + A\frac{a^2}{4}\Delta\omega(\mathbf{x}, t) + O([a^2\Delta]^2), \quad (9)$$

where Δ is the Laplace operator. Since $\nabla \times \omega\hat{z} = -\Delta\mathbf{u}$ and similarly for \mathbf{p} and m , we obtain

$$\mathbf{p} = A\mathbf{u}(\mathbf{x}, t) + A\frac{a^2}{4}\Delta\mathbf{u}(\mathbf{x}, t) + O([a^2\Delta]^2). \quad (10)$$

Inserting Eq. (10) into Eq. (4) for the zeroth-order term yields

$$\begin{aligned} \sigma_{ij}^{a(0)} &= \alpha A^2 \left(u_i u_j - \frac{1}{3} \delta_{ij} \mathbf{u}^2 \right) + \alpha A^2 \frac{a^2}{4} (u_i \Delta u_j + u_j \Delta u_i) \\ &+ \alpha A^2 \frac{a^4}{16} \left(\Delta u_i \Delta u_j - \frac{1}{3} \delta_{ij} (\Delta \mathbf{u})^2 \right) + O([a^2\Delta]^4), \end{aligned} \quad (11)$$

resulting in additional quadratic nonlinearities in Eq. (1), some of which break Galilean invariance. The first term in Eq. (11) leads to a renormalization of the Navier-Stokes nonlinearity and hence to a different Reynolds number. Since the sign of α depends on the type of swimmer with $\alpha < 0$ for pullers and $\alpha > 0$ for pushers, the renormalization of the Reynolds number depends on the type of microswimmers. The second term can be subsumed into the pressure gradient, while remaining terms which are of higher order in the gradients contribute to a redistribution of kinetic energy mostly at small scales. Since all terms conserve the mean kinetic energy and hence do not result in a net energy input, we neglect the additional small-scale nonlinearities, thereby ensuring Galilean invariance. The energy input from the microswimmers hence has to originate from the first-order term in the gradient expansion of the active stresses given in

Eq. (5). Substituting Eq. (10) in Eq. (5) results in

$$\sigma_{ij}^{a(1)} = \beta A \left(1 + \frac{a^2}{4} \Delta + \frac{a^4}{32} \Delta^2 \right) (\partial_i u_j + \partial_j u_i) + O([a^2\Delta]^3), \quad (12)$$

where terms up to order Δ^2 from Eq. (10) have been included in order to ensure the existence of a driving interval in scale that corresponds to the experimentally observed mesoscale vortices induced by the bacterial motion. The structure of $\nabla \cdot \sigma^{a(1)}$ takes on the form of the effective viscosity previously proposed by Słomka and Dunkel [30], provided $\beta > 0$. The latter is the case if \mathbf{p} is chosen to point along the swimming direction and does not depend on the type of microswimmer [40]. If we choose \mathbf{p} to point against the swimming direction, then A should be negative. That is, the product βA is always positive. In what follows, we choose $A > 0$ such that \mathbf{p} points into the same direction as the solvent flow. After the rescaling

$$t \rightarrow t\sqrt{1-\alpha A}, \quad \mathbf{u} \rightarrow \mathbf{u}\sqrt{1-\alpha A}, \quad (13)$$

the resulting two-dimensional one-fluid model reads as

$$\begin{aligned} \partial_t \mathbf{u} + \mathbf{u} \cdot \nabla \mathbf{u} &= -\nabla \Pi + \Gamma \left(\Gamma_0 + \Gamma_2 \Delta + \frac{\Gamma_2^2}{2} \Delta^2 \right) \Delta \mathbf{u}, \\ \nabla \cdot \mathbf{u} &= 0, \end{aligned} \quad (14)$$

where

$$\Gamma = \frac{\beta A}{\sqrt{1-\alpha A}}, \quad \Gamma_0 = 1 + \frac{\nu}{\beta A}, \quad \Gamma_2 = \frac{a^2}{4}. \quad (15)$$

Equation (14) relies upon two main assumptions: (i) \mathbf{u} and \mathbf{p} are divergence free, i.e., the bacterial concentration must be constant and density fluctuations negligible; (ii) the system must be two dimensional, as the reduction to a one-dimensional problem resulting in Eq. (7) is not justified otherwise. Specifically, in three dimensions there is no *a priori* reason to set $G_{ij} = G\delta_{ij}$ in Eq. (6). In summary, Eq. (14) is applicable to dense suspensions of microswimmers in very thin layers, where a 2D approximation is justified. We note that friction with a substrate has been neglected, however, the corresponding term can easily be added.

In this context, the original introduction of the solvent model by Słomka and Dunkel corresponds to setting $G(\mathbf{x}) \sim \delta(\mathbf{x})$ and using certain higher-order terms in the gradient expansion of the active stresses. The former amounts to assuming that the polarization and solvent velocity fields are related only locally and the latter introduces additional parameters. Physically, *locally* means on scales smaller than that of the mesoscale vortices. Here, we obtain a very similar model from a long-range relation between the fields, which is more appropriate in a hydrodynamic context.

Similarly, the bacterial flow model introduced in Ref. [10] can be obtained by formally solving Eq. (1) to obtain $\mathbf{u}[\mathbf{p}]$, or by neglecting \mathbf{u} altogether. Both solvent and bacterial flow models reproduce the experimentally observed spatiotemporally chaotic dynamics characteristic of active matter turbulence [10,11,32] and have been used extensively in investigations thereof [30–35,37,43–47]. They differ in the choice of fields in which the model is expressed, with the consequence that terms originating from the free energy are not explicitly present in the solvent model.

The solvent models resemble the Navier-Stokes equations in their structure and have the key ingredient for an inertial range that is typical of normal turbulence: in the absence of forcing and dissipation, the nonlinear terms in the equation preserve the mean kinetic energy $\langle |\mathbf{u}|^2 \rangle$. We note that in general Galilean invariance is broken by active corrections of the type $\alpha A^2 \frac{a^2}{4} (u_i \Delta u_j + u_j \Delta u_i)$ coming from Eq. (11) to the advective nonlinearity in Eq. (14) that have been neglected here, as the constant Galilean shift is neither canceled by a contribution from another term or removed by spatial gradients. The effects of the active particles are thus concentrated in the effective viscosity in Eq. (14), and we will focus on two variants of the models and discuss similarities and differences to results in the literature that were obtained with the bacterial flow model.

B. Polynomial effective viscosity

The solvent model introduced by Słomka and Dunkel [30] has a stress tensor in Eq. (1) given by a polynomial gradient expansion

$$\sigma_{ij} = (\Gamma_0 + \Gamma_2 \Delta + \Gamma_4 \Delta^2) (\partial_i u_j + \partial_j u_i), \quad (16)$$

and results in a continuous effective viscosity

$$\hat{\nu}(k) = \Gamma_0 - \Gamma_2 k^2 + \Gamma_4 k^4, \quad (17)$$

where $\hat{\nu}$ denotes the Fourier transform. In what follows, we will therefore refer to the combination of Eqs. (1) and (16) as the polynomial effective viscosity (PEV) model.

If $\Gamma_2 < 0$, then Eq. (17) is a combination of normal and hyperviscosity and all terms dissipate energy. If, in contrast, $\Gamma_2 > 0$, there is a wave number interval where $\hat{\nu}(k) < 0$, resulting in a linear amplification of the Fourier modes in that wave number interval. The interplay between this instability and the Navier-Stokes nonlinearity drives spatiotemporal dynamics that for certain values of Γ_i results in the formation of mesoscale vortices and spatial correlations, which resemble the experimental observations [32].

By completing the square, the wave number form of the effective viscosity can be written as

$$\hat{\nu}(k) = \Gamma_0 + \Gamma_4 [(k^2 - k_f^2)^2 - k_f^4] \quad (18)$$

with

$$k_f^2 = \Gamma_2 / (2\Gamma_4) \quad (19)$$

the wave number of the minimum in the viscosity (which is real only for $\Gamma_2 > 0$). With the normalization of wave numbers to k_f , i.e., $\tilde{k} = k/k_f$, the effective viscosity can be written

$$\hat{\nu}(k) = \Gamma_0 \{1 + \gamma [(\tilde{k}^2 - 1)^2 - 1]\}, \quad (20)$$

where

$$\gamma = \Gamma_4 k_f^4 / \Gamma_0 = \frac{\Gamma_2^2}{4\Gamma_0\Gamma_4} = \frac{(\Gamma_2/\Gamma_0)^2}{4(\Gamma_4/\Gamma_0)} \quad (21)$$

is the one remaining parameter that controls the forcing.

The scaled effective viscosity $\hat{\nu}$ has two parameters Γ_0 , which sets the scale for the viscosity and γ , which is a measure for both the amplification and the range of wave

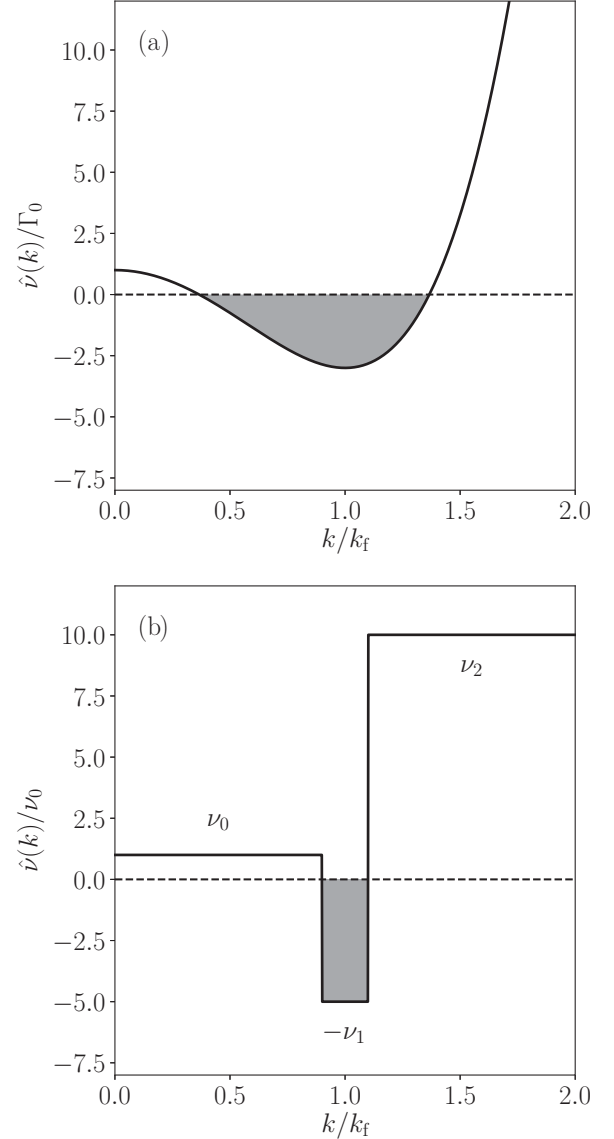


FIG. 1. Effective viscosity for PEV and PCV models. (a) PEV $\hat{\nu}/\Gamma_0$ vs k/k_f . (b) PCV $\hat{\nu}(k)/\nu_0$ vs k/k_f . The gray-shaded area corresponds to the interval $[k_{\min}, k_{\max}]$, where the amplification occurs.

numbers that are forced, as we will now discuss. The effective viscosity attains its minimum at $\tilde{k}^2 = 1$, where

$$\hat{\nu}(\tilde{k} = 1) = \Gamma_0(1 - \gamma). \quad (22)$$

Clearly, $\hat{\nu}$ can become negative, and hence forcing rather than dissipating, for $\gamma > 1$ only. The range of wave numbers over which it is forcing is given by

$$\tilde{k}_{\min}^2 = 1 - \sqrt{1 - \frac{1}{\gamma}} < \tilde{k}^2 < 1 + \sqrt{1 - \frac{1}{\gamma}} = \tilde{k}_{\max}^2, \quad (23)$$

and varies with γ . A sketch of $\hat{\nu}(k)$ for the PEV model is provided in Fig. 1(a), the gray-shaded area indicating the wave number interval where amplification occurs, $\hat{\nu}(k) < 0$. The upper end of the interval approaches 2 for $\gamma \rightarrow \infty$, showing that there will be no forcing on smaller wavelengths, whereas the lower end of the interval approaches 0, indicating that the

driving band extends to ever lower wave numbers and thus larger scales in this limit.

Since the effective viscosity is measured in units of Γ_0 and since the length scale has been fixed as $L_f = \pi/k_f$ all scales in the momentum equation are set: specifically, time is measured in units of L_f^2/Γ_0 and velocity in units of Γ_0/L_f . Introducing that scale, Eq. (1) contains a single parameter γ , with the stress tensor given by

$$\sigma_{ij} = \{1 + \gamma[(1 + \Delta)^2 - 1]\}(\partial_i u_j + \partial_j u_i). \quad (24)$$

Variations in γ should therefore give rise to different dynamics. Słomka and Dunkel [30] discuss statistically steady states for several values of their control parameters Γ_0 , Γ_2 , and Γ_4 , that is, in our notation for different values of γ and corresponding driving scales and amplitudes. Some of these states were multiscale with energy spectra reminiscent of fully developed 2D turbulence [30,35], and small condensates were observed for certain parameter values [35]. One can then expect that stronger large-scale structures may form for more intense driving, but since γ controls not only the strength of the forcing but also the width and the location of the driving band, it is difficult to see which of the effects dominate. This was remedied in the model used in [36] and described next, where amplification and driving scale can be set independently from each other.

C. Piecewise constant viscosity

The piecewise constant viscosity (PCV) model [36] is a discontinuous approximation to the PEV model, with the Navier-Stokes stress tensor written in terms of an effective viscosity given as a set of step functions in Fourier space

$$\hat{\nu}(k) = \begin{cases} \nu_0 > 0 & \text{for } k < k_{\min}, \\ -\nu_1 < 0 & \text{for } k_{\min} \leq k \leq k_{\max}, \\ \nu_2 > 0 & \text{for } k > k_{\max}. \end{cases} \quad (25)$$

The values of ν_i are chosen such that the resulting discrete form of $\hat{\nu}(k)$ resembles the polynomial form of the PEV model. Specifically, ν_1 controls the forcing, and $\nu_2 > \nu_0$ mimics the hyperviscous term in the PEV model. A sketch of $\hat{\nu}(k)$ for the PCV model is provided in Fig. 1(b), the gray-shaded area indicating the wave number interval where amplification occurs, $\hat{\nu}(k) = -\nu_1 < 0$. As in the PEV model, ν_0 sets the scale for the effective viscosity. The PCV model can thus be described by dimensionless parameters for amplification ν_1/ν_0 and small-scale dissipation ν_2/ν_0 . An effective driving scale $L_f = \pi/k_f$ can be defined by the midpoint of the interval $[k_{\min}, k_{\max}]$, i.e., $k_f = (k_{\min} + k_{\max})/2$.

The PCV model approximates the functional form of the PEV model's effective viscosity by a piecewise constant function, remaining faithful to the original PEV model in an important point: the driving is proportional to the velocity field and it is confined to a wave number band. This results in driving through local-in-scale amplification in both cases, i.e., in essentially the same physics. That is, even though the small-scale properties of the velocity fields obtained by the PCV and the original PEV model may differ in some detail, the large-scale and mean properties should be similar, if not the same, as they are dominated by the nonlinearity and not by details of how the driven interval is specified. In this context, we point

out that the functional form of the effective viscosity in any one-equation model is essentially a consequence of the choice of convolution kernel. For a Gaussian filter, one obtains PEV, using a sinc filter in configuration space results in the PCV model with $\nu_2 = \nu_0$. Moreover, a small increase in energy input for a fixed viscosity results in a considerably wider driven interval in the PEV model. In experiments, this would correspond to a significantly wider distribution of vortices for faster microswimmers than for slower microswimmers and correspondingly to much broader energy spectra in the former case than in the latter. We are not aware of experiments testing this, but it would be interesting to compare data from different organisms, for instance, *B. subtilis* versus *E. coli*. Since the driven range is held fixed for the PCV model, it is therefore phenomenologically closer to experiments than the PEV model.

III. DIRECT NUMERICAL SIMULATIONS

The PEV and PCV models are studied in two dimensions, using data generated by numerical integration of the momentum equation in vorticity form

$$\partial_t \hat{\omega}(\mathbf{k}) + [\mathbf{u} \cdot \widehat{\nabla} \omega](\mathbf{k}) = -\hat{\nu}(k) k^2 \hat{\omega}(\mathbf{k}), \quad (26)$$

where ω is the only nonvanishing component of the vorticity, $\nabla \times \mathbf{u}(x, y) = \omega(x, y) \hat{\mathbf{z}}$. Equation (26) is supplemented with either Eq. (18) for PEV or Eq. (25) for the PCV model. In all cases, we use the standard pseudospectral technique [48] on the domain $[0, 2\pi]^2$ with periodic boundary conditions and full dealiasing by truncation following the (2/3)rd rule [49]. The simulations are initialized with random Gaussian-distributed data, or, in case of hysteresis calculations for the PCV model, with data obtained from another run at a different value of the control parameter.

For PCV, two series of simulations were carried out. The first one, PCV-A, consists of a parameter scan in ν_1/ν_0 with all other parameters, i.e., ν_0 , ν_2 , k_{\min} , and k_{\max} held fixed. That is, only the amplification is varied between the simulations in each PCV-A data set. The three simulations of the second series, PCV-B, were done at higher resolution, with parameters chosen such that results can be compared with PCV-A using the scaling properties of the Navier Stokes equations, i.e., PCV-B corresponds to PCV-A in a larger simulation domain. Parameters and observables of all runs are summarized in Table I. The PEV model is investigated for three test cases at lower resolution and subsequently through a series of simulations with fixed scale separation between the domain size and the beginning of the driven interval. Parameters and observables for the PEV model are summarized in Table II. All simulations reach a statistically stationary state, where the total energy per unit volume fluctuates about a mean value, and are subsequently continued for at least 2000 large-eddy turnover times. Prior to that, the system evolves through a transient nonstationary stage. Owing to the absence of a large-scale dissipation mechanism, this can take a long time for certain parameter regimes. During the statistically stationary state, the velocity fields were sampled in intervals of one large-eddy turnover time.

TABLE I. Parameters and observables for all PCV simulations, with N denoting the number of grid points in each coordinate of the simulation domain $[0, 2\pi]^2$, v_0 , v_1 , and v_2 are the parameters defining the PCV model as in Eq. (25) with $v_0 = 0.0011$ for PCV-A and $v_0 = 1.7 \times 10^{-5}$ for PCV-B. The driven intervals are specified by k_{\min} and k_{\max} as defined in Eq. (25) for PCV. The Reynolds number Re is based on the integral scale $L = 2/U^2 \int_0^\infty dk E(k)/k$ and the rms velocity U , and Re_f is the Reynolds number based on the effective driving scale L_f and the velocity in the driven range of scales, ε_{LS} the energy dissipation rate in the interval $[1, k_{\min}]$, ε_{IN} the energy input rate in the interval $[k_{\min}, k_{\max}]$, and ε_{SS} the energy dissipation rate in the interval $(k_{\max}, 2\pi/(N/3)]$. All observables are ensemble averaged during the statistically stationary state, with samples taken at intervals of one large-eddy turnover time $T = L/U$. The asterisk indicates data from Ref. [36].

Run id	N	v_1/v_0	v_2/v_0	k_{\min}	k_{\max}	Re	U	L	Re_f	ε_{LS}	ε_{IN}	ε_{SS}
PCV-A1*	256	0.25	10.0	33	40	19	0.29	0.07	19	0.029	0.048	0.023
PCV-A2*	256	0.5	10.0	33	40	26	0.36	0.085	21	0.056	0.10	0.046
PCV-A3*	256	0.75	10.0	33	40	35	0.39	0.09	21	0.086	0.16	0.071
PCV-A4*	256	1.0	10.0	33	40	44	0.43	0.11	21	0.11	0.21	0.09
PCV-A5*	256	1.25	10.0	33	40	58	0.47	0.13	21	0.15	0.26	0.14
PCV-A6*	256	1.5	10.0	33	40	75	0.52	0.15	20	0.18	0.30	0.16
PCV-A7*	256	1.75	10.0	33	40	106	0.57	0.20	19	0.17	0.34	0.16
PCV-A7a	256	1.75	10.0	33	40	106	0.57	0.20	20	0.18	0.32	0.15
PCV-A8*	256	2.0	10.0	33	40	212	0.66	0.35	19	0.18	0.36	0.18
PCV-A8a	256	2.0	10.0	33	40	227	0.67	0.37	19	0.19	0.34	0.17
PCV-A9*	256	2.02	10.0	33	40	249	0.68	0.40	19	0.18	0.36	0.18
PCV-A9a	256	2.02	10.0	33	40	2686	1.64	1.79	17	0.15	0.28	0.13
PCV-A10*	256	2.04	10.0	33	40	296	0.70	0.46	19	0.18	0.36	0.18
PCV-A10a	256	2.04	10.0	33	40	2957	1.77	1.82	17	0.14	0.28	0.13
PCV-A11*	256	2.083	10.0	33	40	3347	1.95	1.87	17	0.13	0.28	0.15
PCV-A11a	256	2.083	10.0	33	40	3270	1.92	1.85	17	0.14	0.28	0.13
PCV-A12*	256	2.167	10.0	33	40	3708	2.13	1.90	16	0.13	0.27	0.15
PCV-A13*	256	2.25	10.0	33	40	3927	2.24	1.91	16	0.13	0.28	0.15
PCV-A14*	256	2.5	10.0	33	40	4455	2.52	1.92	15	0.12	0.27	0.15
PCV-A15*	256	2.625	10.0	33	40	4636	2.63	1.92	14	0.11	0.26	0.15
PCV-A16*	256	2.75	10.0	33	40	4851	2.75	1.92	14	0.11	0.26	0.15
PCV-A17*	256	2.875	10.0	33	40	5088	2.89	1.92	14	0.11	0.27	0.16
PCV-A18*	256	3.0	10.0	33	40	5313	3.01	1.92	14	0.11	0.28	0.17
PCV-A19*	256	3.25	10.0	33	40	5793	3.28	1.92	14	0.12	0.29	0.18
PCV-A20*	256	3.5	10.0	33	40	6241	3.54	1.92	14	0.13	0.31	0.19
PCV-A21*	256	3.75	10.0	33	40	6708	3.80	1.93	14	0.13	0.33	0.20
PCV-A22*	256	4.0	10.0	33	40	7214	4.08	1.93	14	0.14	0.35	0.22
PCV-A23*	256	4.25	10.0	33	40	7723	4.27	1.93	14	0.16	0.38	0.24
PCV-A24*	256	4.5	10.0	33	40	8230	4.65	1.93	14	0.17	0.40	0.25
PCV-A25*	256	4.75	10.0	33	40	8751	4.95	1.93	14	0.18	0.43	0.27
PCV-A26*	256	5.0	10.0	33	40	9258	5.24	1.93	14	0.19	0.46	0.29
PCV-A27	256	5.25	10.0	33	40	9690	5.51	1.92	15	0.21	0.53	0.32
PCV-A28*	256	5.5	10.0	33	40	10286	5.81	1.93	15	0.23	0.57	0.34
PCV-A29*	256	6.0	10.0	33	40	11416	6.44	1.93	15	0.27	0.65	0.39
PCV-A30*	256	6.5	10.0	33	40	12530	7.08	1.93	15	0.31	0.74	0.44
PCV-A31*	256	7.0	10.0	33	40	13677	7.77	1.93	16	0.36	0.84	0.49
PCV-B1*	1024	1.0	10.0	129	160	45	0.027	0.029	21	0.0001	0.00019	9×10^{-5}
PCV-B2*	1024	2.0	10.0	129	160	226	0.041	0.094	20	0.00017	0.00033	0.00016
PCV-B3*	1024	5.0	10.0	129	160	132914	1.17	1.93	15	0.00018	0.00046	0.00026

IV. MODEL DYNAMICS

We begin our study of the properties of the models by tracking the time evolution of the total kinetic energy per unit volume $E(t)$ given by the difference between input and dissipation,

$$\frac{dE}{dt} = \varepsilon_{\text{IN}}(t) - [\varepsilon_{\text{LS}}(t) + \varepsilon_{\text{SS}}(t)], \quad (27)$$

where the input ε_{IN} , the large-scale dissipation ε_{LS} , and the small-scale dissipation ε_{SS} are obtained by integrating the

effective viscosity over the respective wave number ranges, i.e., calculated as

$$\varepsilon_{\text{IN}}(t) = \int_{k_{\min}}^{k_{\max}} dk \int d\hat{\mathbf{k}} \hat{v}(k) k^2 |\hat{\mathbf{u}}(\mathbf{k}, t)|^2, \quad (28)$$

$$\varepsilon_{\text{LS}}(t) = \int_0^{k_{\min}} dk \int d\hat{\mathbf{k}} \hat{v}(k) k^2 |\hat{\mathbf{u}}(\mathbf{k}, t)|^2, \quad (29)$$

$$\varepsilon_{\text{SS}}(t) = \int_{k_{\max}}^{\infty} dk \int d\hat{\mathbf{k}} \hat{v}(k) k^2 |\hat{\mathbf{u}}(\mathbf{k}, t)|^2, \quad (30)$$

TABLE II. Parameters and observables for all PEV simulations, with N denoting the number of grid points in each coordinate of the simulation domain $[0, 2\pi]^2$. The model parameters in Eq. (18) are $\Gamma_0 = 0.0011$ for the PEV series and $\Gamma_0 = 0.0002725$ for the PEV-64 series, Γ_2/Γ_0 and Γ_4/Γ_0 resulting in $I = \int_{k_{\min}}^{k_{\max}} \hat{v}(k) dk$, with the driven intervals specified by k_{\min} and k_{\max} as defined in Eq. (23) for PEV. The Reynolds number Re is based on the integral scale $L = 2/U^2 \int_0^\infty dk E(k)/k$ and the rms velocity U , and Re_f is the Reynolds number based on the effective driving scale L_f and the velocity in the driven range of scales, ε_{LS} the energy dissipation rate in the interval $[1, k_{\min})$, ε_{IN} the energy input rate in the interval $[k_{\min}, k_{\max}]$, and ε_{SS} the energy dissipation rate in the interval $(k_{\max}, 2\pi/(N/3)]$. All observables are ensemble averaged during the statistically stationary state, with samples taken at intervals of one to three large-eddy turnover time $T = L/U$.

Run id	N	I	Γ_2/Γ_0	Γ_4/Γ_0	k_{\min}	k_{\max}	Re	U	L	Re_f	ε_{IN}	ε_{LS}	ε_{SS}
PEV-1	256	0.21	0.002	7.72×10^{-7}	26	43	14	0.10	0.15	5	0.002	0.0012	0.0008
PEV-2	256	0.31	0.0023	9.26×10^{-7}	23	45	68	0.22	0.35	9	0.0072	0.0044	0.0028
PEV-3	256	0.93	0.0025	9.65×10^{-7}	22	45	668	0.66	1.56	10	0.0155	0.0097	0.0056
PEV-64-1	512	0.00578	0.0003076	1.55×10^{-8}	64	126	34	0.09	0.10	8	0.0083	0.0050	0.0033
PEV-64-2	512	0.00586	0.0003072	1.54×10^{-8}	64	126	50	0.09	0.12	8	0.0086	0.0051	0.0034
PEV-64-3	512	0.00595	0.0003069	1.53×10^{-8}	64	126	65	0.10	0.14	9	0.0089	0.0053	0.0036
PEV-64-4	512	0.00604	0.0003065	1.52×10^{-8}	64	127	70	0.11	0.18	9	0.0093	0.0056	0.0037
PEV-64-5	512	0.00613	0.0003062	1.51×10^{-8}	64	127	109	0.12	0.25	9	0.0096	0.0058	0.0039
PEV-64-7	512	0.00614	0.0003061	1.51×10^{-8}	64	127	140	0.12	0.31	9	0.0097	0.0058	0.0039
PEV-64-7	512	0.00616	0.0003061	1.51×10^{-8}	64	127	170	0.13	0.36	9	0.0098	0.0058	0.0039
PEV-64-8	512	0.00617	0.0003060	1.51×10^{-8}	64	127	247	0.14	0.47	9	0.0098	0.0059	0.0039
PEV-64-9	512	0.00619	0.0003059	1.51×10^{-8}	64	127	282	0.15	0.51	9	0.0099	0.0059	0.0039
PEV-64-10	512	0.00622	0.0003058	1.51×10^{-8}	64	127	389	0.17	0.63	9	0.0100	0.0060	0.0040
PEV-64-11	512	0.00631	0.0003055	1.50×10^{-8}	64	128	719	0.24	0.81	9	0.0104	0.0062	0.0042
PEV-64-12	512	0.00641	0.0003051	1.49×10^{-8}	64	128	980	0.30	0.88	9	0.0108	0.0065	0.0044

with $\hat{k} = k/k$ a unit vector in direction of k . During statistically stationary evolution, mean energy input must equal mean energy dissipation, $\varepsilon_{IN} = \varepsilon = \varepsilon_{LS} + \varepsilon_{SS}$. The characteristics of the nonstationary evolution depends on the presence of an inverse energy transfer. If an inverse cascade is present, as in fully developed 2D turbulence, it can be expected that $E(t)$ grows linearly in time as long as ε_{LS} is negligible. This is a consequence of the fact that the dynamics at the small scales is much faster than at large scales leading to $\varepsilon_{IN} \simeq \text{const}$ and $\varepsilon_{SS} \simeq \text{const}$, and one obtains

$$E(t) \simeq (\varepsilon_{IN} - \varepsilon_{SS})t, \quad (31)$$

until ε_{LS} becomes sufficiently large. This equation holds as long as $\varepsilon_{LS} \approx 2\nu_0 E(t) L(t)^{-2}$ is negligible compared to $\varepsilon_{IN} - \varepsilon_{SS} \approx 2\nu_1 E_{IN} L_f^{-2} - \varepsilon_{SS}$. Neglecting ε_{SS} , one must have $\varepsilon_{IN} \gg \varepsilon_{LS}$ resulting in $(\nu_1/\nu_0) E_{IN} L_f^{-2} \gg E(t) L(t)^{-2}$, where $L(t) = \pi/k(t)$ denotes the length scale corresponding to the maximum of $E(k, t)$. That is, Eq. (31) describes the dynamics to a good approximation on timescales $t \ll ((\nu_1/\nu_0) E_{IN} L_f^{-2})^{-1/2}$. For later times, when fluctuations on the largest available scale are excited, i.e., when $L(t) = L_{\text{box}}$, Eq. (27) results in

$$\frac{dE}{dt} = \varepsilon_{IN} - \varepsilon_{SS} - \varepsilon_{LS}(t) \approx \varepsilon_{IN} - \varepsilon_{SS} - 2\nu_0 E(t) L_{\text{box}}^{-2}, \quad (32)$$

such that $E(t)$ saturates exponentially

$$E(t) \approx \frac{\varepsilon_{IN} - \varepsilon_{SS}}{2\nu_0 L_b^{-2}} - e^{-t/\tau} \quad (33)$$

on the viscous timescale $\tau = 1/(2\nu_0 L_{\text{box}}^{-2})$ [50].

The time evolution of $E(t)$ is shown in Fig. 2 for representative cases. Figure 2(a) contains the results for the runs PCV-B1, PCV-B2, and PCV-B3 with amplification factors $\nu_1/\nu_0 = 1$, $\nu_1/\nu_0 = 2$, and $\nu_1/\nu_0 = 5$, respectively. Figure 2(b) shows

the corresponding results for PEV with parameters $\Gamma_2/\Gamma_0 = 0.0025$, $\Gamma_2/\Gamma_0 = 0.0023$, and $\Gamma_2/\Gamma_0 = 0.002$, with Γ_4 chosen such that the forcing remains centered around $k_f = 36$.

The behavior of $E(t)$ is qualitatively similar for the two models and differs between the respective example cases. The two cases with low amplification, that is, $\nu_1/\nu_0 = 1$ and $\nu_1/\nu_0 = 2$ for PCV and $\Gamma_2/\Gamma_0 = 0.002$ and $\Gamma_2/\Gamma_0 = 0.0023$ for PEV become statistically stationary and fluctuate around relatively low mean values of E . In contrast, for the cases $\nu_1/\nu_0 = 5$ for PCV and $\Gamma_2/\Gamma_0 = 0.0025$ for PEV, the kinetic energy grows at first linearly, which is characteristic of a nonstationary inverse energy cascade in 2D turbulence [51]. This is followed by statistically stationary evolution, where $E(t)$ fluctuates about mean values which are an order of magnitude larger than for the aforementioned cases. In absence of a large-scale friction term, once an inverse energy transfer is established, statistical stationarity can only be realized through the development of a condensate at the largest scales.

Compared with the energy levels of the PCV cases shown in Fig. 2(a), the energy levels of the PEV runs shown in Fig. 2(b) are much lower. As can be seen from the values listed in Table I, the driven interval is much wider in PEV than it is in PCV, such that more nonlinear interactions are taking place within and close to the driven interval. That is, the nonlinear transfer is more efficient in redistributing energy across scales in PEV than it is in PCV. Furthermore, the effective viscosity is smaller in PEV than in PCV close to the driven interval, that is, less energy is dissipated there. The consequence of the two effects is that in PEV less energy input is necessary to reach statistically stationary states with multiscale dynamics and, eventually, with a condensate. This can also be seen by comparing the energy input rates listed in Table I.

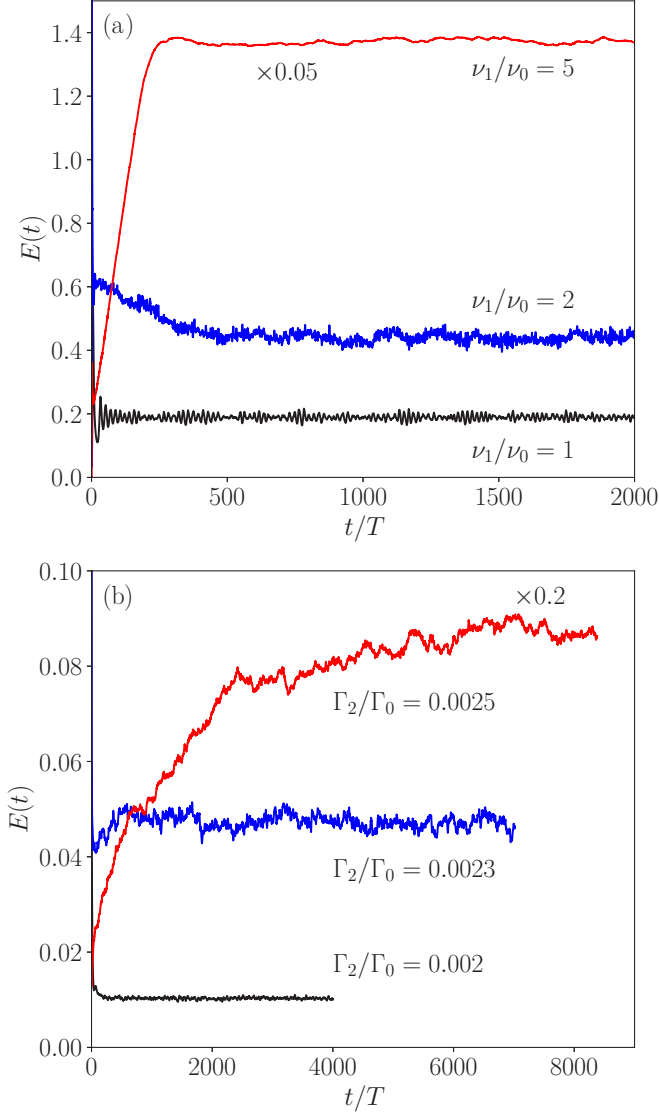


FIG. 2. Time evolution of the total kinetic energy per unit volume for three example cases for PCV (a) and PEV (b). The energy has been divided by a factor of 20 for the PCV case $\nu_1/\nu_0 = 5$ and by a factor of 5 for the PEV case $\Gamma_2/\Gamma_0 = 0.0025$ in order to improve the readability of the figure.

Emergence of large-scale structures

The formation of successively larger structures and the eventual formation of a condensate with increasing amplification can be seen in visualizations of the velocity field, as given in [36]. Here, we provide visualizations of ω for the three PCV cases in Fig. 3. The vorticity fields for $\nu_1/\nu_0 = 1$ and $\nu_1/\nu_0 = 2$ are similar, with the vortices in the latter case slightly stronger and a bit larger. Finally, for $\nu_1/\nu_0 = 5$ a condensate manifests itself in form of two counter-rotating vortices as in classical 2D turbulence [27,51].

The emergence of large-scale organization and coherence can be quantified through the calculation of equal-time correlation functions. Owing to isotropy, it is sufficient to consider the two-point longitudinal correlator

$$C_{LL}(r) = \langle u_L(\mathbf{x} + \mathbf{r})u_L(\mathbf{x}) \rangle, \quad (34)$$

where $r = |\mathbf{r}|$, and $u_L = \mathbf{u} \cdot \mathbf{r}/r$ is the velocity component along the displacement vector \mathbf{r} , and the angled brackets denote a combined spatial and temporal average. Longitudinal correlation functions have been calculated through the spectral expansions of the respective velocity fields for PCV and PEV, with results shown in Fig. 4, where PCV and PEV data are contained in the Figs. 4(a) and 4(b), respectively. Clear correlations up to the size of the system can be identified for $\nu_1/\nu_0 = 5$ and $\Gamma_2/\Gamma_0 = 0.0025$, while C_{LL} decreases much faster in r for the cases without a condensate, $\nu_1/\nu_0 = 1$, $\nu_1/\nu_0 = 2$, $\Gamma_2/\Gamma_0 = 0.002$, and $\Gamma_2/\Gamma_0 = 0.0023$. In all cases, anticorrelations are present. For the weakly forced cases shown in black and blue (dark gray) in Fig. 4 these are barely visible in comparison to the condensate.

The differences in correlation can also be quantified with the integral scale

$$L \equiv \frac{1}{C_{LL}(0)} \int_0^\infty dr C_{LL}(r), \quad (35)$$

listed in Table I: There is at least an $O(10)$ difference between the respective values of L for PCV-B3 and the two cases with less amplification, PCV-B1 and PCV-B2, and similarly for PEV.

V. TRANSITION

The transition between the two cases $\nu_1/\nu_0 = 1$ and 2 without a condensate and $\nu_1/\nu_0 = 5$ with a condensate is discontinuous, as shown in [36]. This discontinuous transition between spatiotemporal chaos and classical 2D turbulence suggests that the two states are separated by a subcritical bifurcation. Accordingly, we expect to find a bistable scenario with the possibility of coexisting states in a parameter range around the transition, and eventually also hysteresis. As observable we take the energy at the largest scale E_1 , which will be considered as a function of the amplification factor and the energy input. E_1 is calculated in terms of the energy spectrum

$$E(k) \equiv \left\langle \frac{1}{2} \int d\hat{\mathbf{k}} |\hat{\mathbf{u}}(\mathbf{k})|^2 \right\rangle_t, \quad (36)$$

where $\int d\hat{\mathbf{k}}$ indicates an average over all angles in k space with prescribed $|\mathbf{k}| = k$ and $\langle \cdot \rangle_t$ denotes a time average during statistically steady evolution. E_1 is then given by $E_1 = E(k)|_{k=1}$. Following our analysis in Ref. [36], Fig. 5 presents E_1 as a function of ν_1/ν_0 close to the critical point. Two main features of the transition can be identified in the figure. First, E_1 increases suddenly at the critical value $\nu_1/\nu_0 = 2.00 \pm 0.02$, as observed in Ref. [36]. Second, the system shows hysteretic behavior: the red (gray) curve consists of data points obtained for decreasing ν_1/ν_0 , while the black curve corresponds to states obtained for increasing ν_1/ν_0 . The resulting hysteresis loop is clearly visible.

Apart from the presence of hysteresis shown here, the expected bistable scenario is realized in the statistically stationary total energy balance

$$\varepsilon = \varepsilon_{\text{IN}} \simeq 2\nu_0 \frac{(2\pi)^2}{L_f^2} E_{\text{IN}}, \quad (37)$$

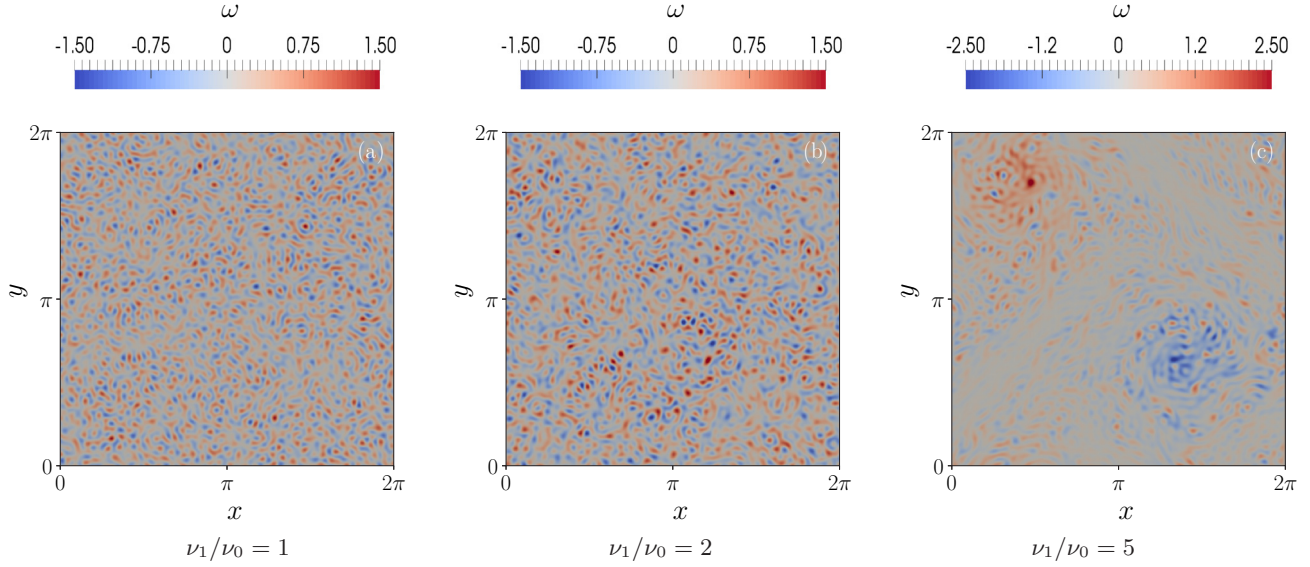


FIG. 3. Visualization of the vorticity field $\omega(x, y)\hat{z}$ for PCV cases $\nu_1/\nu_0 = 1$ (a), $\nu_1/\nu_0 = 2$ (b), and $\nu_1/\nu_0 = 5$ (c) using samples taken during the statistically stationary state.

where

$$E_{\text{IN}} = \int_{k_{\text{min}}}^{k_{\text{max}}} dk E(k), \quad (38)$$

with an upper and a lower branch of ε as a function of E_{IN} corresponding to classical 2D turbulence with an emerging condensate and spatiotemporal chaos at the forcing scale, respectively [36]. The two branches were found to be connected by an unstable S-shaped region. The existence of two branches connected by an S-shaped region is also visible in the phase-space projection relating the energy at the largest scale to the energy input, i.e., for E_1 as a function of ε_{IN} as shown in Fig. 6(a). The lower branch corresponds to injection rates obtained for $\nu_1/\nu_0 < \nu_{1,\text{crit}}/\nu_0$, where E_1 is negligible and the inverse transfer is damped by dissipation at intermediate scales before reaching the largest scale in the system. On the upper branch that describes states with a sizable condensate, we observe a linear relation between E_1 and ε_{IN} , as can be expected if most energy is dissipated in the condensate

$$\varepsilon_{\text{IN}} = \varepsilon \simeq 2\nu_0 E_1 k_1^2 \Delta k, \quad (39)$$

where $k_1 = 1$ is the lowest wave number in the domain, and $\Delta k = 1$ the width of the wave number shell centered at k_1 .

The S-shaped region in Fig. 6(a) can only occur if ε_{IN} is a nonmonotonous function of the amplification factor. This is indeed the case as can be seen in Fig. 6(b), where a sudden decrease in ε_{IN} occurs at $\nu_{1,\text{crit}}/\nu_0$, followed by an interval in ν_1/ν_0 where ε_{IN} varies very little. Eventually, for states with a condensate ε_{IN} increases linearly with ν_1/ν_0 . The nature of the transition is thus related to nonmonotonous behavior of the energy input (and therefore the dissipation) as a function of the control parameter, which can only occur if the energy input depends on the velocity field. In particular, for Gaussian-distributed and δ -in-time correlated forcing ε_{IN} itself is the control parameter and a scenario as described here is unlikely to occur. This observation suggests that the

type of transition depends on the type of forcing, that is, it is nonuniversal.

As explained in Sec. II B, the structure of the PEV model precludes a parameter study with fixed driving scale and energy input range, as variations in the energy input or the amplification factor Γ_2 invariably lead to a variation in the width of the forcing band. One can either fix the scale separation between the domain size and the driven range of scales by fixing k_{min} , with the consequence that k_{max} and location k_f of the maximum of $\hat{v}(k)$ vary, or one fixes k_f and the scale separation varies with energy input or amplification factor. That is, a parameter scan cannot result in like-for-like comparisons between simulations as the location of a critical point most likely depends on the location and width of the driven interval. In order to carry out at least a systematic investigation into the PEV model, we introduce a new control parameter

$$I = \int_{k_{\text{min}}}^{k_{\text{max}}} \hat{v}(k) dk. \quad (40)$$

For the PCV model, I is proportional to the amplification factor ν_1 , as the width of the driven interval is held constant. As such, using I as a control parameter comes closest to a like-for-like comparison with the parameter study for the PCV model.

The PEV parameter study was carried out on 256^2 and 512^2 lattice points, and we could not find hysteresis as shown in Fig. 7 using the series PEV-64 summarized in Table II. However, we found transiently coexisting statistically stationary states with different values of the kinetic energy at the largest scale in the system E_1 . These intermediate states can remain for about 2000 large-eddy turnover times as shown for an exemplary calculation in Fig. 8(a). To observe the eventual collapse, the simulations have to be continued to more than 8000 large-eddy turnover times as shown in Fig. 8(b). For comparison with experimental conditions we identify L_f with the typical size of a mesoscale vortex and measure velocities

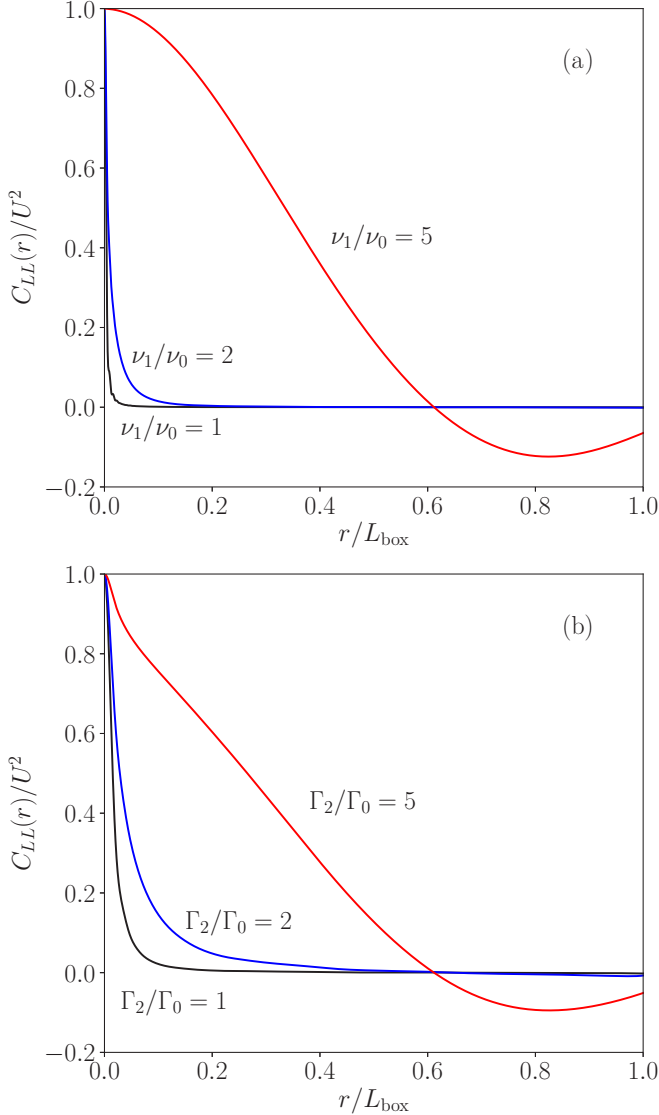


FIG. 4. Longitudinal correlation functions. (a) PCV for different values of ν_1/ν_0 . (b) PEV for different values of Γ_2/Γ_0 . The color coding and the values for ν_1/ν_0 and for Γ_2/Γ_0 correspond to data shown in Fig. 2.

in $\mu\text{m/s}$ as in Ref. [36], resulting run times of about 30 min for the intermediate states and 7 h to eventually observe the single, final flow state. The latter may become difficult to observe in experimental conditions, as the microswimmers will eventually slow down owing to oxygen depletion of their environment.

To compare to experimental data and between the two models, we define a Reynolds number based on the effective driving scale L_f and the velocity at the driven scales

$$\text{Re}_f = \frac{\sqrt{E_{\text{IN}}} L_f}{\tilde{\nu}}, \quad (41)$$

where $\tilde{\nu}$ is the Newtonian viscosity, i.e., $\tilde{\nu} = \nu_0$ for PCV and $\tilde{\nu} = \Gamma_0$ for PEV. This Reynolds number corresponds to the Reynolds number associated with the mesoscale vortices observed in experiments. Values of Re_f for all simulations are given in Table I. The transition occurs at $\text{Re}_f \simeq 20$ for

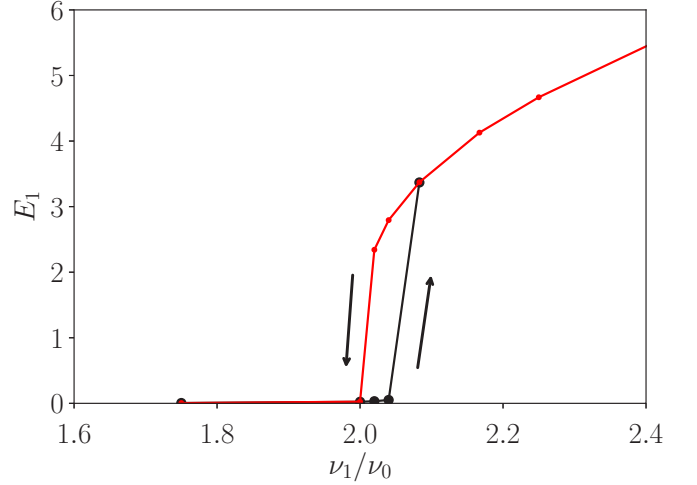


FIG. 5. E_1 as a function of ν_1/ν_0 . The black curve corresponds to flow states obtained by increasing ν_1/ν_0 and the red (gray) curve to flow states obtained by decreasing ν_1/ν_0 . A hysteresis loop is visible in the region $2.00 \leq \nu_1/\nu_0 \leq 2.04$.

PCV and at $\text{Re}_f \simeq 10$ for PEV, the exact value may depend on simulation details such as the width of the driving range and the level of small-scale dissipation. However, the main point is that both models transition at Reynolds number of $O(10)$. In comparison, the experimentally observed Reynolds numbers are about $O(10^{-2})$, based on characteristic vortex sizes of $100 \mu\text{m}$, with a characteristic speed of $100 \mu\text{m/s}$ for *B. subtilis* [2], and the kinematic viscosity of water $\nu_{\text{H}_2\text{O}} = 10^{-6} (\mu\text{m})^2/\text{s}$.

A. Spectral scaling

Energy spectra for PCV and PEV are shown Figs. 9(a) and 9(b), respectively. The dotted lines in Fig. 9(a) correspond to series PCV-A, and the solid lines to rescaled PCV-B data as in Ref. [36]. The transition can be located clearly in the spectra as E_1 increases by three orders of magnitude from the third to the fourth dotted line. The PEV energy spectra presented in Fig. 9(b) correspond to $\Gamma_2/\Gamma_0 = 0.0025$ (red), $\Gamma_2/\Gamma_0 = 0.0023$ (blue), and $\Gamma_2/\Gamma_0 = 0.002$ (black), with the forcing centered around $k_f = 36$ as in the PCV model. The results are similar to those for the PCV model shown Fig. 9(a) in terms of spectral scaling and the formation of the condensate. However, the condensate appears more gradually in PEV than it does in PCV and the energy in the driven range is a monotonic function in PEV while being nonmonotonic in PCV. Energy spectra with an extended scaling range and a small accumulation of energy at the smallest wave number have also been observed in the bacterial flow model [34]. There, the critical amplification rate at which the condensate occurs will depend on the relaxation term $-\alpha_F \mathbf{p}$ that originates from the functional derivative of the free energy given in Eq. (3). Indeed, the existence of a critical value of $\alpha_F > 0$, below which no energy accumulation occurs, has been reported in Ref. [31]. Similarly, condensate formation in Newtonian turbulence can be suppressed in presence of sufficiently strong linear friction [52]. In view of the transition

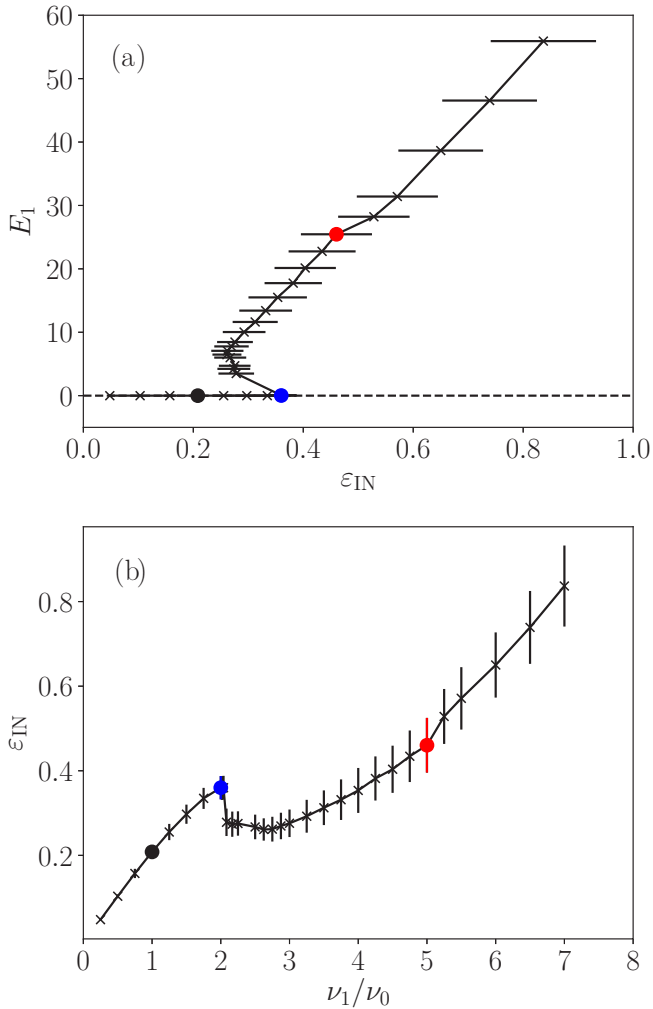


FIG. 6. (a) E_1 as a function of ϵ_{IN} . (b) ϵ_{IN} as a function of ν_1/ν_0 . The red (light gray), blue (dark gray), and black dots correspond to the PCV cases discussed in Sec. IV. The horizontal lines in (a) and the vertical lines (b) show the standard error on ϵ_{IN} , which was calculated by taking samples at intervals of one large-eddy turnover time during statistically steady evolution.

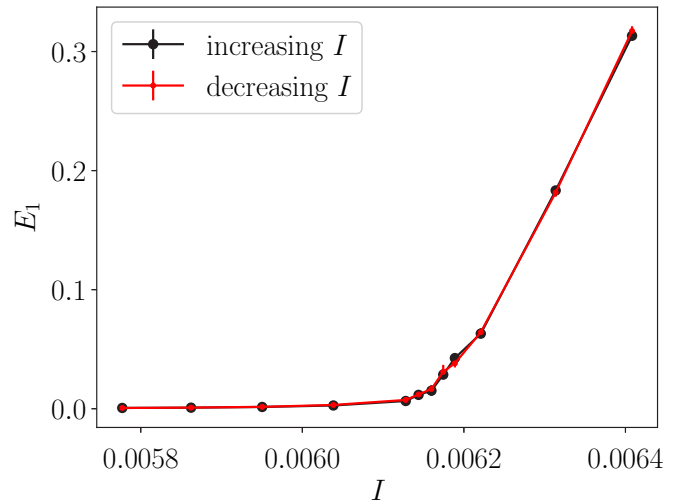


FIG. 7. E_1 as a function of I for series PEV-64. The black curve corresponds to flow states obtained by increasing I and the red (gray) curve to flow states obtained by decreasing I .

scenarios, a general quantification of the effect of large-scale dissipation would be of interest.

At low amplification, equipartition scaling $E(k) \propto k$ is observed for PEV and PCV, as indicated by the black curves in Fig. 9. In contrast, the low wave number form of $E(k)$ is nonuniversal for the bacterial flow model even at very low amplification [31]. This difference also originates from the presence of the relaxation term $-\alpha_F p$ in the bacterial flow model, in Ref. [31] the scaling exponent of $E(k)$ at $k < k_{min}$ is found to depend on α_F . In Newtonian turbulence, deviations from Kolmogorov scaling of $E(k)$ also depend on details of large-scale dissipation such as the strength of a linear friction term or the use of hypoviscosity [52].

Further observations can be made from the data shown in Fig. 9. The spectral exponent is larger than the Kolmogorov value of $-\frac{2}{3}$ even in presence of an inverse energy transfer, resulting in shallower spectra. This can have several reasons. For simulations with a small condensate such as for the PEV

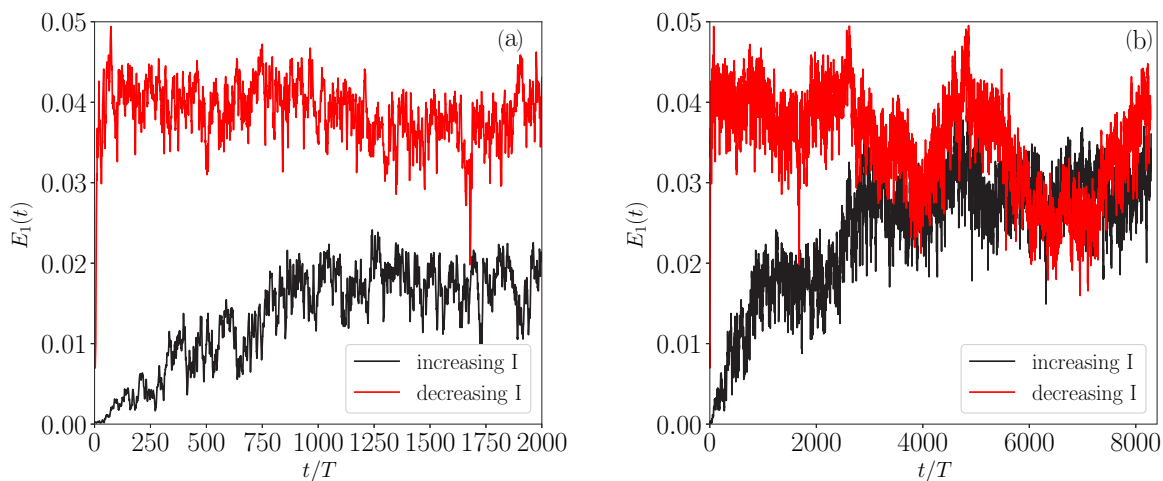


FIG. 8. E_1 as a function of t for run PEV-64-4. The black curve corresponds to flow states obtained by increasing I and the red (gray) curve to flow states obtained by decreasing I . (a) Short evolution times, (b) full time series.

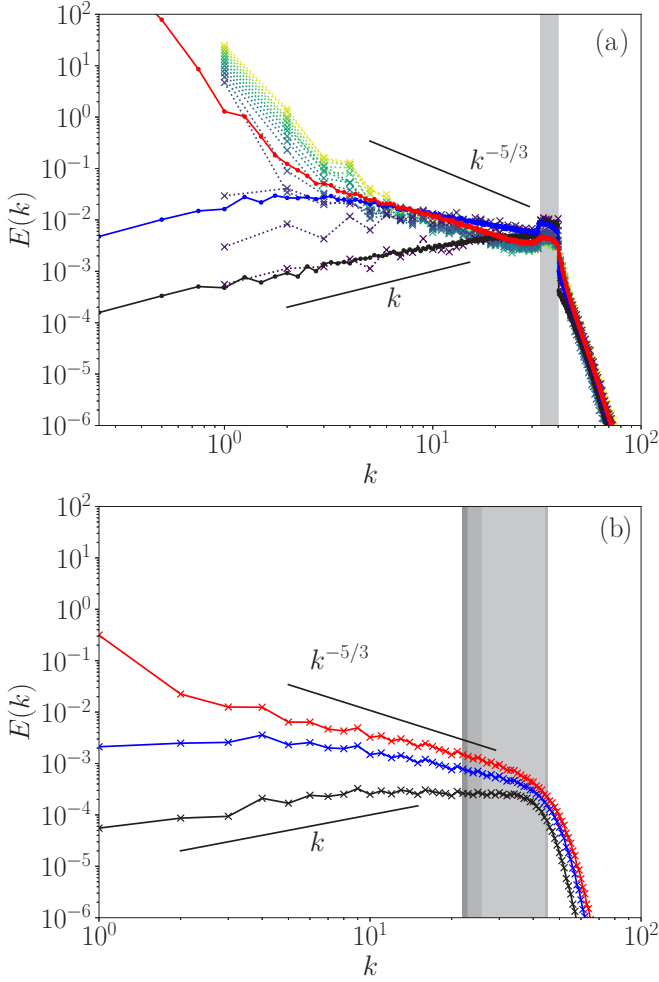


FIG. 9. Energy spectra. (a) PCV with for different values of ν_1/ν_0 . The solid lines show the rescaled PCV-B cases $\nu_1/\nu_0 = 1$ (black), $\nu_1/\nu_0 = 2$ (blue), and $\nu_1/\nu_0 = 5$ (red), and the dotted lines PCV-A data. (b) PEV with $\Gamma_2/\Gamma_0 = 0.0025$ (red), $\Gamma_2/\Gamma_0 = 0.0023$ (blue), and $\Gamma_2/\Gamma_0 = 0.002$ (black). The gray-shaded areas indicate the respective driving ranges.

data set with $\Gamma_2/\Gamma_0 = 0.0025$ shown in red (light gray) in Fig. 9(b), energy dissipation is not negligible in the wave number range between the condensate and the driven interval, and Kolmogorov's hypotheses do not apply. For simulations with a sizable condensate such as PCV-B3 shown in red (light gray) in Fig. 9(a), the condensate itself alters the dynamics in the inertial range. In presence of a condensate, the spectral scaling is known to become steeper [53], with $E(k) \propto k^{-3}$ for the entire wave number range $k < k_{\min}$. Removing the coherent part of the velocity field results in shallower scaling $E(k) \propto k^{-1}$ [53]. Intermediate states with spectra similar to PCV-B3 have also been obtained [see Fig. 3(A) in Ref. [53]].

B. Nonlocal transfers

Since the driving in both models depends on the amount of energy in the driven range, a reduction in the energy input with *increasing* amplification requires a reduction in E_{IN} . One way by which this could happen is through an enhanced nonlinear

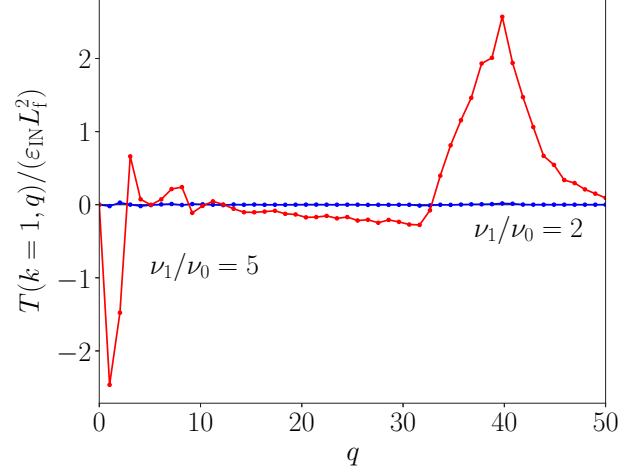


FIG. 10. PCV shell-to-shell transfer function $T(k, q)/(\epsilon_{\text{IN}} L_f^2)$ for $k = 1$ and $1 \leq q \leq 50$. Blue (dark gray): $\nu_1/\nu_0 = 2$, without condensate. Red (light gray): $\nu_1/\nu_0 = 5$, with condensate at $k = 1$.

transfer out of the driven wave number range. The reduction in E_{IN} occurs at the critical point, which suggests that the condensate may couple directly to the driven scales, leading to a nonlocal spectral energy transfer from the driven wave number interval into the condensate. In order to investigate whether this is the case, the energy transfer spectrum was decomposed into shell-to-shell transfers [31,54,55] between linearly spaced spherical shells centered at wave numbers k and q :

$$T(k, q) = \left\langle \int d\hat{k} \int d\hat{q} \int dp \hat{u}_k^* \cdot (\hat{u}_p \cdot i\hat{q}) \hat{u}_q \delta(\mathbf{k} + \mathbf{p} - \mathbf{q}) \right\rangle_t, \quad (42)$$

where \hat{k} and \hat{q} are unit vectors. Here, the focus is on the existence of a coupling between the condensate and the driven scales, hence, linear shell spacing is sufficient. More quantitative statements concerning the relative weight of different couplings within the overall transfer requires logarithmic spacing [56]. Figure 10 shows the nondimensional energy transfer into the lowest wave number shell $T(k, q)/(\epsilon_{\text{IN}} L_f^2)$ for $k = 1$, for the two example cases PCV-A8 (without condensate) and PCV-A26 (with condensate). In the first case, $T(k = 1, q) \approx 0$ for all q , that is, there is no net nonlocal energy transfer from the driven scales to the largest scales. In contrast, in the second case, $T(k = 1, q)$ has a clear maximum around $q = k_{\max} = 40$, hence, energy is transferred from the driven scales into the condensate bypassing the intermediate scales. The data for PCV-A26 also show a forward transfer from the $k = 1$ shell into the $q = 2$ shell, as $T(k = 1, q)$ has a distinctive minimum at $q = 2$ and is negative.

VI. FOUR-SCALE MODEL

Some of the qualitative features of the transition can be captured in a four-scale model. The main motivation for the construction of which is to try to understand if a nonlocal coupling between the driven scales and the condensate reproduces the observations from the DNS parameter scan. From the shell-to-shell transfers calculated for two example

cases discussed in the previous section, we know that energy is transferred nonlocally between the condensate and the driven scales, however, we cannot deduce if and how such nonlocal couplings are responsible for the phenomenology of the transition.

Let E_{LS} be the energy content at the intermediate wave numbers $1 < k < k_{\min}$ and E_{SS} the energy content at $k > k_{\max}$. Then, one can consider the interaction of the four quantities E_1 , E_{IN} , E_{LS} , and E_{SS} :

$$\dot{E}_1 = -2\nu_0 k_1^2 E_1 + c_3 E_1^{1/2} E_{LS} + c_2 \theta(E_1 - E_{1,0})(E_1 - E_{1,0})^{1/2} E_{IN}, \quad (43)$$

$$\dot{E}_{LS} = -2\nu_0 k_{LS}^2 E_{LS} + c_1 E_{LS}^{1/2} E_{IN} - c_3 E_1^{1/2} E_{LS}, \quad (44)$$

$$\dot{E}_{IN} = 2\nu_1 k_{IN}^2 E_{IN} - c_1 E_{LS}^{1/2} E_{IN} - c_4 E_{SS}^{1/2} E_{IN} - c_2 \theta(E_1 - E_{1,0})(E_1 - E_{1,0})^{1/2} E_{IN}, \quad (45)$$

$$\dot{E}_{SS} = -2\nu_2 k_{SS}^2 E_{SS} + c_4 E_{SS}^{1/2} E_{IN}, \quad (46)$$

where θ is the Heaviside step function, $c_i > 0$ for $i = 1, \dots, 4$ parametrize the coupling terms, and $k_1 = 1$, k_{LS} , k_{IN} , and k_{SS} are effective wave numbers in the corresponding ranges. In terms of energy transfers, the coupling terms represent

$$E_{IN} \longrightarrow E_{LS} : c_1 E_{LS}^{1/2} E_{IN}, \quad (47)$$

$$E_{IN} \longrightarrow E_1 : c_2 \theta(E_1 - E_{1,0})(E_1 - E_{1,0})^{1/2} E_{IN}, \quad (48)$$

$$E_{LS} \longrightarrow E_1 : c_3 E_1^{1/2} E_{LS}, \quad (49)$$

$$E_{IN} \longrightarrow E_{SS} : c_4 E_{SS}^{1/2} E_{IN}, \quad (50)$$

where the coupling between E_{IN} and E_1 is modeled such that a nonlocal energy transfer from the driven wave number range into the largest resolved scales only takes place once a condensate is emerging. The coupling parameters c_i can be obtained from DNS data through calculations of shell-to-shell nonlinear transfers. Once they are known, a parameter scan in ν_1 can be carried out for different values of the threshold energy $E_{1,0}$ in order to compare the results from the model with the DNS data. However, before doing so, we derive predictions from the model equations for two asymptotic cases:

(i) presence of a condensate $E_1 \gg E_{1,0}$, corresponding to the upper branch in Fig. 6,

(ii) absence of a condensate $E_1 < E_{1,0}$, corresponding to the lower branch in Fig. 6.

In what follows, the small-scale dissipation is neglected, as this enables us to focus on the main points. We will come back to an analysis of the full model in Sec. VIA.

Case (i): $E_1 \gg E_{1,0}$. For $E_1 \gg E_{1,0}$ we approximate the coupling term between E_{IN} and E_1 as

$$c_2 \theta(E_1 - E_{1,0})(E_1 - E_{1,0})^{1/2} E_{IN} \simeq c_2 E_1^{1/2} E_{IN}, \quad (51)$$

and we neglect the coupling term $c_3 E_1^{1/2} E_{LS}$ that describes a local energy transfer from the intermediate scales into the condensate. The latter is introduced to model the nonlocal contribution to the inverse energy transfer in presence of a condensate as discussed in Sec. VB. Equations (43)–(45) then

simplify to

$$\dot{E}_{IN} = 2\nu_1 k_{IN}^2 E_{IN} - c_1 E_{LS}^{1/2} E_{IN} - c_2 E_1^{1/2} E_{IN}, \quad (52)$$

$$\dot{E}_{LS} = -2\nu_0 k_{LS}^2 E_{LS} + c_1 E_{LS}^{1/2} E_{IN}, \quad (53)$$

$$\dot{E}_1 = -2\nu_0 k_1^2 E_1 + c_2 E_1^{1/2} E_{IN}, \quad (54)$$

which result in the following expressions for E_{IN} , E_{LS} , and E_1 in steady state:

$$2\nu_1 k_{IN}^2 E_{IN} = c_1 E_{LS}^{1/2} E_{IN} + c_2 E_1^{1/2} E_{IN} \Rightarrow c_1 E_{LS}^{1/2} + c_2 E_1^{1/2} = -2\nu_1 k_{IN}^2, \quad (55)$$

$$2\nu_0 k_{LS}^2 E_{LS} = c_1 E_{LS}^{1/2} E_{IN} \Rightarrow E_{LS} = \left(\frac{c_1}{2\nu_0 k_{LS}^2} E_{IN} \right)^2, \quad (56)$$

$$2\nu_0 k_1^2 E_1 = c_2 E_1^{1/2} E_{IN} \Rightarrow E_1 = \left(\frac{c_2}{2\nu_0 k_1^2} E_{IN} \right)^2. \quad (57)$$

Solving for E_{IN} as a function of ν_1 , one obtains

$$2\nu_1 k_{IN}^2 = c_1 E_{LS}^{1/2} + c_2 E_1^{1/2} = \frac{c_1^2}{2k_{LS}^2} + \frac{c_2^2}{2k_1^2} E_{IN} \Rightarrow E_{IN} = -4 \frac{\nu_1 \nu_0 k_{IN}^2}{\frac{c_1^2}{k_{LS}^2} + \frac{c_2^2}{k_1^2}}, \quad (58)$$

that is, $E_{IN} \sim \nu_1$ and $E_1 \sim \nu_1^2$, in qualitative agreement with the data presented in Fig. 3 of Ref. [36] for $\nu_1 > \nu_{1,\text{crit}}$, respectively.

Case (ii): $E_1 < E_{1,0}$. In this case, there is no nonlocal coupling between E_1 and E_{IN} , hence, Eqs. (43)–(45) become

$$\dot{E}_{IN} = 2\nu_1 k_{IN}^2 E_{IN} - c_1 E_{LS}^{1/2} E_{IN}, \quad (59)$$

$$\dot{E}_{LS} = -2\nu_0 k_{LS}^2 E_{LS} + c_1 E_{LS}^{1/2} E_{IN} - c_3 E_1^{1/2} E_{LS}, \quad (60)$$

$$\dot{E}_1 = -2\nu_0 k_1^2 E_1 + c_3 E_1^{1/2} E_{LS}, \quad (61)$$

which leads the following expressions in steady state:

$$2\nu_1 k_{IN}^2 E_{IN} = c_1 E_{LS}^{1/2} E_{IN} \Rightarrow E_{LS} = \left(\frac{2\nu_1 k_{IN}^2}{c_1} \right)^2, \quad (62)$$

$$2\nu_0 k_{LS}^2 E_{LS} = c_1 E_{LS}^{1/2} E_{IN} - c_3 E_1^{1/2} E_{LS} \Rightarrow E_{IN} = \frac{1}{c_1} (2\nu_0 k_{LS}^2 + c_3 E_1^{1/2}) E_{LS}^{1/2}, \quad (63)$$

$$2\nu_0 k_1^2 E_1 = c_3 E_1^{1/2} E_{LS} \Rightarrow E_1 = \left(\frac{c_3}{2\nu_0 k_1^2} E_{LS} \right)^2. \quad (64)$$

Solving for E_{IN} as a function of ν_1 , one obtains

$$E_{IN} = 4 \frac{\nu_1 \nu_0}{c_1^2} k_{IN}^2 \left[k_{LS}^2 + \left(\frac{c_3 \nu_1 k_{IN}^2}{c_1 \nu_0 k_1} \right)^2 \right], \quad (65)$$

while $E_1 \sim \nu_1^4$.

Comparing the energy content in the driven wave number range between cases (i) and (ii) given in Eqs. (58) and (65), respectively, we find

$$E_{\text{IN}}^{\varepsilon_+} = 4 \frac{\nu_1 \nu_0 k_{\text{IN}}^2}{\frac{c_1^2}{k_{\text{LS}}^2} + \frac{c_2^2}{k_1^2}} < 4 \frac{\nu_1 \nu_0}{c_1^2} k_{\text{IN}}^2 \left[k_{\text{LS}}^2 + \left(\frac{c_3 \nu_1 k_{\text{IN}}^2}{c_1 \nu_0 k_1} \right)^2 \right] = E_{\text{IN}}^{\varepsilon_-}. \quad (66)$$

We point out that this comparison is only justified close to the critical point, as in principle the different cases imply different ranges of ν_1 : case (i) is applicable for $\nu_1 > \nu_{1,\text{crit}}$ and case (ii) for $\nu_1 < \nu_{1,\text{crit}}$. However, in the vicinity of $\nu_{1,\text{crit}}$, Eq. (66) predicts a sudden drop in E_{IN} and therefore of $\varepsilon_{\text{IN}} = 2\nu_1 k_{\text{IN}}^2 E_{\text{IN}}$ as a function of ν_1 , which is indeed observed in the DNS data as shown in Fig. 6(b). In summary, the asymptotics of the model predicts qualitative features of the transition which are in agreement with the DNS results. For further quantitative results, we evaluate the model numerically.

Parameter scan for ν_1

The results of the previous sections demonstrate that the four-scale model is able to qualitatively reproduce the features of flow states above and below the critical value of ν_1 . In order to obtain the properties of the transition to a condensate in the model system, we now proceed with a parameter scan. The full model given by Eqs. (43)–(46) is integrated numerically for each value of ν_1 . The values of the coefficients c_i , for $1 \leq i \leq 4$, have been chosen based on the values of shell-to-shell transfers [31,54] from DNS data above and below the critical point,

$$c_1 = \frac{T(k = k_{\text{LS}}, p = k_{\text{IN}}, q \simeq k_1)}{\sqrt{E_{\text{LS}} E_{\text{IN}}}} = 0.037, \quad (67)$$

$$c_2 = \frac{T(k = k_1, p = k_{\text{IN}}, q \simeq k_{\text{IN}})}{\sqrt{E_1 E_{\text{IN}}}} = 0.043, \quad (68)$$

$$c_3 = \frac{T(k = k_1, p = k_{\text{LS}}, q \simeq k_{\text{LS}})}{\sqrt{E_1 E_{\text{LS}}}} = 0.0031, \quad (69)$$

$$c_4 = \frac{T(k = k_{\text{SS}}, p = k_{\text{IN}}, q \simeq k_1)}{\sqrt{E_{\text{SS}} E_{\text{IN}}}} = 0.84, \quad (70)$$

where $k_1 = 1$, $k_{\text{LS}} = 5$, $k_{\text{IN}} = 12$, and $k_{\text{SS}} = 20$. The qualitative behavior of the model, which we discuss in what follows, does not depend on the value of $E_{1,0}$ or on the values of c_1, \dots, c_4 as long as all $c_i \neq 0$. A change in parameters would locate the transition at a different value of ν_1 . Here, we choose a cutoff value $E_{1,0} = 0.05$, which results in a transition in the interval $0 < \nu_1 < 1$.

A sharp transition must occur in the four-scale model as the dynamics change at the threshold value $E_{1,0}$ whose qualitative features are remarkably similar to the transition in the full system. Figure 11 presents the results of the parameter scan for E_1 [Figs. 11(a) and 11(c)] and ε_{IN} [Figs. 11(b) and 11(d)] as functions of ν_1 [Figs. 11(a) and 11(b)] and E_{IN} [Figs. 11(c) and 11(d)]. As in the full system, E_1 shows a sudden jump at a critical value of ν_1 and thereafter increases quadratically in

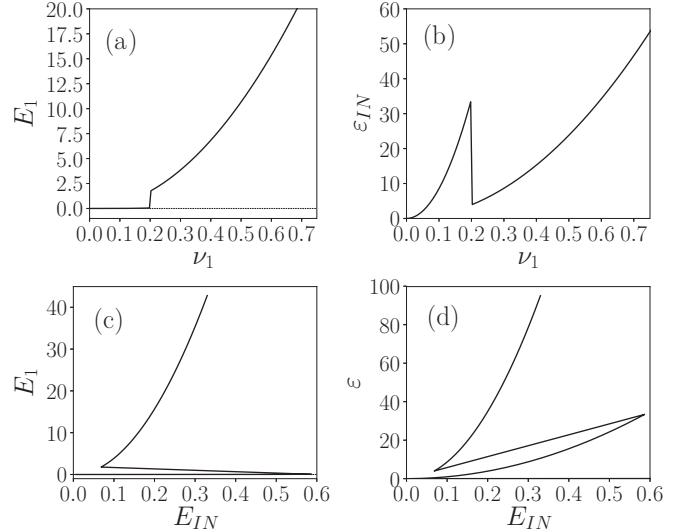


FIG. 11. E_1 (left) and ε_{IN} (right) as functions of ν_1 (top row) and E_{IN} (bottom row) calculated from a parameter scan of Eqs. (43)–(46) and for $E_{1,0} = 0.05$.

ν_1 , while E_{IN} drops suddenly as predicted for the asymptotic cases in Secs. VI 1 and VI 2.

Furthermore, different states of the model system may be realized at the same value of ν_1 , as can be seen Figs. 11(b) and 11(d), where E_1 and ε are presented as functions of E_{IN} . The sharp transition is present in form of a discontinuity in the data along a critical line, and for both E_1 and ε we observe S-shaped curves with upper and lower branches and an unstable region in-between. This is qualitatively similar to the behavior of the full system, as can be seen by comparison with Fig. 6(a), which presents the corresponding DNS data for $E_1(\nu_1/\nu_0)$ and with Fig. 3 of Ref. [36] that presents $\varepsilon(\nu_1/\nu_0)$. We point out that the model system is not able to track the second, continuous, transition from absolute equilibrium to viscously damped nonlinear transfers described in Ref. [36], which occurs in the full system at the continuous inflection point of the lower branch ε^- . Such an inflection point is not present in the corresponding model data presented in Fig. 11(d). This is not surprising as the four-scale model is by construction not able to produce equipartition of energy between all degrees of freedom at $k < k_{\text{min}}$.

In summary, the model system adequately reproduces the qualitative features of the transition. More precisely, we can (i) understand the nonmonotonic behavior of the energy content at the driven scales, (ii) understand the scaling of E_1 with ν_1 on the upper branch, and (iii) clearly distinguish the transition to condensate formation from the onset of an inverse energy transfer through postulating a threshold value for E_1 . The transition is present in the model by construction, where the model dynamics becomes nonlocal if a threshold energy at the largest scale is reached. As such, we suggest that the transition in the full system also happens through a similar nonlocal coupling scenario: Energy increases at the largest scales through the classical inverse energy cascade and once a threshold energy is crossed, these emerging large-scale fluctuations couple directly to the energy injection range and a condensate forms.

VII. CONCLUSIONS

Active suspensions can be described by a class of one-fluid models that resemble the Navier-Stokes equation supplemented by active driving provided by small-scale instabilities originating from active stresses exerted on the fluid by the microswimmers. Here, we provided a justification of the one-fluid approach for the two-dimensional case by relating the solvent's velocity field nonlocally to the coarse-grained polarization field of the active constituents. The resulting model is very similar in structure to solvent models postulated on phenomenological grounds [30,32]. The justification relies on two main assumptions: the system must be two-dimensional at least to a good approximation and the bacterial concentration must remain constant. That is, it is applicable to dense suspensions in thin layers.

Numerical simulations of a variant of these models showed that a sharp transition occurs between the formation of a steady-state condensate at the largest length scale in the system and a steady-state inverse transfer which is damped by viscous dissipation before reaching the condensate [36]. The in-depth investigation carried out here supplements the results of Ref. [36], the system is bistable and shows hysteresis. That is, 2D active matter turbulence and 2D hydrodynamic turbulence with a condensate are two nonequilibrium steady states that can coexist in certain parameter ranges and that are connected through a subcritical transition.

The condensate was found to couple directly to the velocity field fluctuations at the driven scales. This observation led to the introduction of a low-dimensional model that includes such a direct nonlinear coupling once a threshold energy at the largest scales is reached. Analytical and numerical evaluations of the model resulted in a good qualitative agreement with DNS results concerning the main features of the transition. As such, we suggest that the nature of the transition is related to correlations between small- and large-scale velocity fluctuations.

Concerning the nature of the transition, we point out that in systems where the energy input depends on the amount of energy at the driving scales, a reduction in input occurs at the critical point. The latter would not be the case for Gaussian-distributed and δ -in-time correlated random forces as the time-averaged energy input is known *a priori*. In that case, preliminary results suggest the occurrence of a supercritical transition (work in progress). This suggests that the transition to developed 2D turbulence is highly nonuniversal: depending on the type of forcing there may be no transition, or it may be subcritical or supercritical. Similar situations occur in rotating flows [57–59]. Subcritical transitions also occur in thin fluid layers as a function of the aspect ratio [60].

Several aspects of our results merit further investigation. First and foremost, it would be of interest to study transitional behavior experimentally. The Reynolds number necessary for the transition that we found here is at least an order of magnitude larger than those describing mesoscale vortices in dense bacterial suspensions. Hence, a further increase of swimming speed, a decrease in viscosity, or a larger driving scale are required to trigger the transition. All three possibilities present considerable difficulty. The most promising approach may be through the use of nonbiological microswimmers such as Janus particles, camphor boats, or magnetic rotors. Second, the effect of friction with a substrate, which is present not only in experiments of active suspensions but also in the Newtonian case, on the location of the critical point needs to be quantified.

ACKNOWLEDGMENTS

With great sadness we report that Bruno Eckhardt passed away on 7 August 2019. We benefited from his astute insights and many interesting discussions in the course of completion of this paper. G.B. acknowledges financial support by the Departments of Excellence grant (MIUR). MCM was supported by the National Science Foundation through Award No. DMR-1609208.

-
- [1] X.-L. Wu and A. Libchaber, *Phys. Rev. Lett.* **84**, 3017 (2000).
 - [2] C. Dombrowski, L. Cisneros, S. Chatkaew, R. E. Goldstein, and J. O. Kessler, *Phys. Rev. Lett.* **93**, 098103 (2004).
 - [3] A. Bricard, J. B. Caussin, N. Desreumaux, O. Dauchot, and D. Bartolo, *Nature (London)* **503**, 95 (2013).
 - [4] T. Sanchez, D. N. Chen, S. J. DeCamp, M. Heymann, and Z. Dogic, *Nature (London)* **491**, 431 (2012).
 - [5] S. Zhou, A. Sokolov, O. D. Lavrentovich, and I. S. Aranson, *Proc. Natl. Acad. Sci. USA* **111**, 1265 (2014).
 - [6] L. Giomi, *Phys. Rev. X* **5**, 031003 (2015).
 - [7] A. Sokolov, I. S. Aranson, J. O. Kessler, and R. E. Goldstein, *Phys. Rev. Lett.* **98**, 158102 (2007).
 - [8] L. H. Cisneros, R. Cortez, C. Dombrowski, R. E. Goldstein, and J. O. Kessler, *Exp. Fluids* **43**, 737 (2007).
 - [9] C. W. Wolgemuth, *Biophys. J.* **95**, 1564 (2008).
 - [10] H. H. Wensink, J. Dunkel, S. Heidenreich, K. Drescher, R. E. Goldstein, H. Löwen, and J. M. Yeomans, *Proc. Natl. Acad. Sci. USA* **109**, 14308 (2012).
 - [11] J. Dunkel, S. Heidenreich, K. Drescher, H. H. Wensink, M. Bär, and R. E. Goldstein, *Phys. Rev. Lett.* **110**, 228102 (2013).
 - [12] J. Gachelin, A. Rousselet, A. Lindner, and E. Clement, *New J. Phys.* **16**, 025003 (2014).
 - [13] U. Frisch, *Turbulence: The Legacy of A. N. Kolmogorov* (Cambridge University Press, Cambridge, 1995).
 - [14] L. D. Landau and E. M. Lifshitz, *Fluid Mechanics* (Pergamon, London, 1959).
 - [15] B. Lautrup, *Physics of Continuous Matter* (CRC Press, Boca Raton, FL, 2005).
 - [16] K. Avila, D. Moxey, A. de Lozar, M. Avila, D. Barkley, and B. Hof, *Science* **333**, 192 (2011).
 - [17] Y. Hatwalne, S. Ramaswamy, M. Rao, and R. A. Simha, *Phys. Rev. Lett.* **92**, 118101 (2004).
 - [18] T. B. Liverpool and M. C. Marchetti, *Phys. Rev. Lett.* **97**, 268101 (2006).
 - [19] A. Sokolov and I. S. Aranson, *Phys. Rev. Lett.* **103**, 148101 (2009).

- [20] J. Gachelin, G. Miño, H. Berthet, A. Lindner, A. Rousselet, and E. Clément, *Phys. Rev. Lett.* **110**, 268103 (2013).
- [21] H. M. López, J. Gachelin, C. Douarche, H. Auradou, and E. Clément, *Phys. Rev. Lett.* **115**, 028301 (2015).
- [22] M. C. Marchetti, *Nature* **525**, 37 (2015).
- [23] V. A. Martinez, E. Clément, J. Arlt, C. Douarche, A. Dawson, J. Schwarz-Linek, A. K. Creppy, V. Škultéty, A. N. Morozov, H. Auradou, and W. C. K. Poon, *Proc. Natl. Acad. Sci. USA* **117**, 2326 (2020).
- [24] G. Kokot, S. Das, R. G. Winkler, G. Gompper, I. S. Aranson, and A. Snezhko, *Proc. Natl. Acad. Sci. USA* **114**, 12870 (2017).
- [25] R. H. Kraichnan, *Phys. Fluids* **10**, 1417 (1967).
- [26] M. Hossain, W. H. Matthaeus, and D. Montgomery, *J. Plasma Phys.* **30**, 479 (1983).
- [27] L. M. Smith and V. Yakhot, *Phys. Rev. Lett.* **71**, 352 (1993).
- [28] A. Alexakis and L. Biferale, *Phys. Rep.* **767-769**, 1 (2018).
- [29] T. B. Liverpool and M. C. Marchetti, in *Cell Motility*, edited by P. Lenz (Springer, Berlin, 2008), pp. 177–206.
- [30] J. Słomka and J. Dunkel, *Eur. Phys. J. Spec. Top.* **224**, 1349 (2015).
- [31] V. Bratanov, F. Jenko, and E. Frey, *Proc. Natl. Acad. Sci. USA* **112**, 15048 (2015).
- [32] J. Słomka and J. Dunkel, *Proc. Natl. Acad. Sci. USA* **114**, 2119 (2017).
- [33] M. James, W. J. T. Bos, and M. Wilczek, *Phys. Rev. Fluids* **3**, 061101(R) (2018).
- [34] A. Oza, S. Heidenreich, and J. Dunkel, *Eur. J. Phys. E* **39**, 97 (2016).
- [35] O. Mickelin, J. Słomka, K. J. Burns, D. Lecoanet, G. M. Vasil, L. M. Faria, and J. Dunkel, *Phys. Rev. Lett.* **120**, 164503 (2018).
- [36] M. Linkmann, G. Boffetta, M. C. Marchetti, and B. Eckhardt, *Phys. Rev. Lett.* **122**, 214503 (2019).
- [37] J. Dunkel, S. Heidenreich, M. Bär, and R. E. Goldstein, *New J. Phys.* **15**, 045016 (2013).
- [38] R. A. Simha and S. Ramaswamy, *Phys. Rev. Lett.* **89**, 058101 (2002).
- [39] L. Giomi, M. C. Marchetti, and T. B. Liverpool, *Phys. Rev. Lett.* **101**, 198101 (2008).
- [40] A. Baskaran and M. C. Marchetti, *Proc. Natl. Acad. Sci. USA* **106**, 15567 (2009).
- [41] P. Constantin, *J. Stat. Phys.* **90**, 571 (1998).
- [42] A. Celani, M. Cencini, A. Mazzino, and M. Vergassola, *New J. Phys.* **6**, 72 (2004).
- [43] P. Srivastava, P. Mishra, and M. C. Marchetti, *Soft Matter* **12**, 8214 (2016).
- [44] E. Putzig, G. S. Redner, A. Baskaran, and A. Baskaran, *Soft Matter* **12**, 3854 (2016).
- [45] J. Słomka and J. Dunkel, *Phys. Rev. Fluids* **2**, 043102 (2017).
- [46] A. Doostmohammadi, T. N. Shendruk, K. Thijssen, and J. M. Yeomans, *Nat. Comm.* **8**, 15326 (2017).
- [47] M. James and M. Wilczek, *Eur. Phys. J. E* **41**, 21 (2018).
- [48] S. A. Orszag, *Phys. Fluids* **12**, II-250 (1969).
- [49] S. A. Orszag, *J. Atmos. Sci.* **28**, 1074 (1971).
- [50] C.-K. Chan, D. Mitra, and A. Brandenburg, *Phys. Rev. E* **85**, 036315 (2012).
- [51] G. Boffetta and R. E. Ecke, *Annu. Rev. Fluid Mech.* **44**, 427 (2014).
- [52] S. Danilov and D. Gurarie, *Phys. Rev. E* **63**, 061208 (2001).
- [53] M. Chertkov, C. Connaughton, I. Kolokolov, and V. Lebedev, *Phys. Rev. Lett.* **99**, 084501 (2007).
- [54] J. A. Domaradzki and R. S. Rogallo, *Phys. Fluids A* **2**, 413 (1990).
- [55] A. Alexakis, P. D. Mininni, and A. Pouquet, *Phys. Rev. E* **72**, 046301 (2005).
- [56] H. Aluie and G. L. Eyink, *Phys. Fluids* **21**, 115108 (2009).
- [57] A. Alexakis, *J. Fluid Mech.* **769**, 46 (2015).
- [58] N. Yokoyama and M. Takaoka, *Phys. Rev. Fluids* **2**, 092602(R) (2017).
- [59] K. Seshasayanan and A. Alexakis, *J. Fluid Mech.* **841**, 434 (2018).
- [60] A. van Kan and A. Alexakis, *J. Fluid Mech.* **864**, 490 (2019).